LRP 614/98 July 1998

SUPPORT OF MODELLING OF MHD EVOLUTION OF DISRUPTIONS, EDDY CURRENTS AND HALO CURRENTS

A. PLETZER

FINAL REPORT — VHTP TASK AGREEMENT
S19 TD 04 97-01-27 FE
NET/97-447, ERB5004 CT970027

Final VHTP report: May 1997 — May 1998

A. Pletzer

Centre de Recherches en Physique des Plasmas, Association Euratom - Confédération Suisse

Presently detached under a VHTP agreement to:

ITER-JCT

11025 N. Torrey Pines Rd., La Jolla CA 92037

pletzea@iterus.org

I. FOREWORD

In the past year I have devoted my energy in three directions. Accordingly, this report contains three distinct parts.

First I have investigated the stability properties of ITER equilibria within the framework of the neoclassical tearing mode theory. This theory [1,2] suggests that the main driving mechanism in the creation of magnetic island is not the free energy as measured by the stability index Δ' ($\equiv$ jump in the logarithmic derivative of the the radial magnetic perturbation), but rather the suppression of bootstrap current resulting from the flattening of the pressure profile as the island grows. Most tokamaks have now routinely observed these modes, which are associated with the observation of soft β limits.

In neoclassical tearing mode theory, the drive originating from the bootstrap current is such that when $-p'/q' > 0$ there is no stable fixed point *unless* $\Delta' < 0$. The saturated island width w is then approximately proportional to $(-\Delta')^{-1}$, whereas no saturation mechanism exists when $\Delta' > 0$.

Experimentally, neoclassical tearing modes tend to develop at the mode rational surfaces 3/2, 2/1 and 4/3, where Δ' tends to be weak. Islands with corresponding resonant poloidal and toroidal mode numbers are, however, not persistently observed and the general understanding is that the island width needs to exceed a particular threshold to form.

This threshold could be overcome by a magnetic perturbation following a sawtooth crash, for instance. There are two models which are presently competing to explain the existence of such a threshold, one based on finite perpendicular transport [3] and the other on the effect of the polarization current [4]. The theory by Wilson *et al.* appears at present to be favoured by experimentalists [5].

If we assume that ITER will be in a sawtooth regime [6] then it is likely that this threshold will be overcome. The so-formed magnetic island could then lead to a significant reduction in the maximum attainable β [7]. However, there are other stabilizing effects which come into play. In § II it is shown that the modification of the equilibrium current profile due to the island amounts to a $w \log w$ term [8] in the evolution equation. Such a contribution dominates over the generally adopted term proportional to w [9], and could explain why modes with $\Delta' > 0$ do not necessarily lead to a disruption.

Even so, the inclusion of the quasi-linear stabilizing effect in the island equation can still produce large saturated island of width in excess of $> 10\%$ of the minor radius in ITER, this due to a combination of weak Δ' and strong bootstrap current near the 2/1 rational surface. To further mitigate the growth of the island, it has recently been proposed to aim a modulated electron cyclotron current drive (ECCD) [10–12] at the O-point of the island in order to overcome the bootstrap current deficit. This scheme relies on good synchronization. Another approach investigated in § III consists in tailoring the current profile by using a continuous ECCD in the neighbourhood of the rational surface so as to decrease Δ'. A substantial stabilization can be achieved for both schemes even for moderate ECCD intensities because stability depends on the gradient of the current density rather than on its magnitude.

The third subject I have tackled concerns disruptions and in particular the determination of the halo and eddy currents during a vertical displacement event (VDE). There is some concern at ITER that the asymmetric component in these currents can lead to large and localized stresses. The important parameters here are the toroidal peaking factor (TPF) [13] and the ratio of halo current to plasma current before the disruption I_h/I_{p0}. It can

be shown by using simple geometrical arguments [14] that these two parameters are in fact inversely correlated (see Fig. 1).

The computation of the halo and eddy currents requires a three-dimensional nonlinear resistive MHD code using a finite element expansion in both radial and poloidal directions. (Previous attempts to use a Fourier expansion in the poloidal direction led to bad convergence when the plasma approached the wall). There are mainly two contenders, MH3D and NIMROD. However, none of these codes have implemented a resistive wall boundary condition at present. I have thus been led to reformulate in § IV A the resistive wall problem in terms of Green's functions in a way that can be used in either codes. The representation of the magnetic field in the vacuum is based on the scalar potential representation, which applies also to $n = 0$ modes provided one takes into account the multi-valued character of the potential in this case. By doing so I have found a new form for the toroidal Green's functions, which are expressed in terms of the hypergeometric function. I have written a code, WALL, which has been tested in the cylindrical limit and I have spent my time recently discussing with my NIMROD co-workers the best way to implement these new boundary conditions.

In the mean time, Tom Gianakon and Carl Sovinec have included the possibility to use a combination of structured mesh (made of quadrilaterals), which is numerically efficient, and an unstructured mesh made of triangles in the region where flux surfaces are open. This new feature will require further testing.

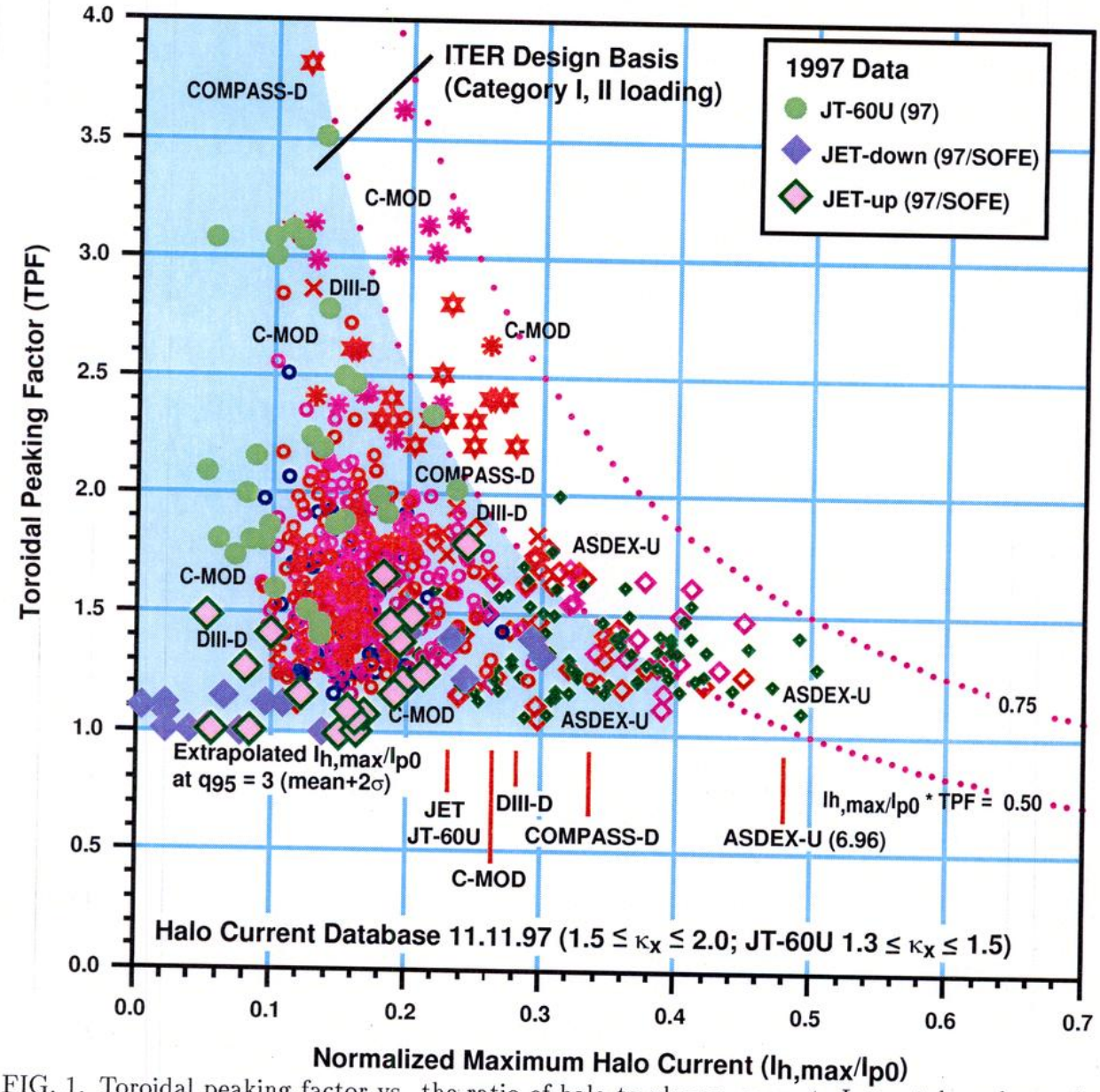

FIG. 1. Toroidal peaking factor vs. the ratio of halo to plasma current. Large tokamaks tend to have a smaller TPF I_h/I_{p0} product (design basis for ITER is 0.5). Courtesy of John Wesley.

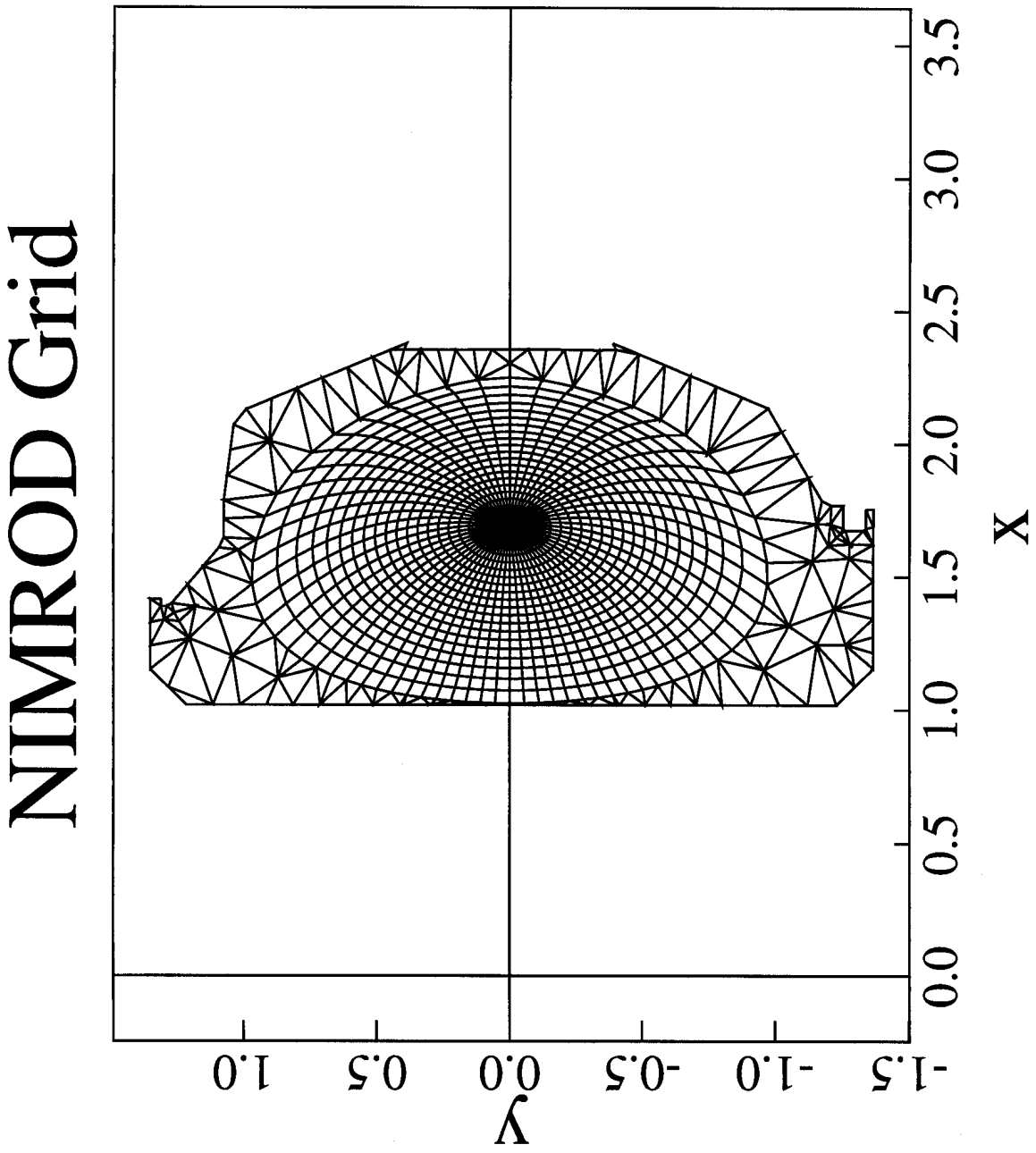

FIG. 2. Structured and unstructured mesh in NIMROD.

II. QUASI-LINEAR STABILIZATION FOR THE ISLAND EVOLUTION EQUATION

Quasi-linear corrections are the result of profile modifications that occur in the course of a magnetic island growth. In a low β plasma, the divergence-free condition for the current density J along the toroidal angle implies that J is approximately a function of the helical flux ψ only. Thus, as the island grows, a region where J is flat forms at the O-point. This in turn removes some of the free energy available to the mode, thereby producing a stabilizing effect.

The problem of estimating the current gradient stabilization has been previously tackled by several authors [9,8,15]. The present work follows more closely the approach of Thyagaraja [8], except that the effect is evaluated in the outer region, where the mode satisfies the zero-frequency ideal magnetohydrodynamic equation [16,17]. Both approaches are consistent and give the same $w \log w$ dependence in the (normalized) island width w. The rational surface where the island develops is a regular singular point in the outer region equation and the solution there can be written in terms of a large and small Frobenius solution [18], i.e an expansion with leading fractional power. The origin of the $w \log w$ dependence lies in the mingling of the small Frobenius solution with the next order term of the large solution. Note that this only occurs when one takes the small β limit.

Chang *et al.* [19] have used a different definition for Δ' based on the jump in logarithmic derivative *evaluated at the half-island width.* The so obtained $\Delta(w)$ can be shown to be essentially equivalent to Δ' with the quasi-linear corrections, both exhibiting the $w \log w$ behaviour.

Other authors [9,8,15] have found a w dependence, which appears to be in contradiction with the present results. A closer inspection of their results reveals, however, that their coefficient of proportionality is related to the average slope of the magnetic perturbation on either side of the rational surface. But it is widely recognized that this coefficient becomes infinite in the $w \to 0$ limit, when $\beta = 0$. This precisely because of the presence of a

logarithmic term in the Frobenius expansion so that this discrepancy is only apparent.

A. Flattening in the inner layer

A plasma of periodicity $2\pi R$ and magnetic field

$$\mathbf{B} = B_z\hat{\mathbf{z}} + \hat{\mathbf{z}}\times\boldsymbol{\nabla}\psi$$

is considered in the large aspect ratio limit. Here,

$$\psi = \psi_0 + A\cos m\hat{\theta} \tag{1}$$

is the helical flux composed of an equilibrium part

$$\psi_0 = \int^r dr B_\theta \left(1 - \frac{q(r)}{q_s}\right) = -B_\theta \frac{q_s'}{q_s}\frac{x^2}{2} + \mathcal{O}(x^3) \quad ; \; x \equiv r - r_s$$

and a small perturbation, which is resonant

$$\hat{\theta} \equiv \theta - \frac{1}{q_s}\frac{z}{R}$$

at the mode rational surface, i.e. where $q(r_s) \equiv q_s = m/n$, m and n being the poloidal and toroidal mode numbers, respectively. Introducing the normalized helical flux

$$s \equiv \tfrac{1}{2}\left(1 - \psi/A\right),$$

Eq.(1) then becomes

$$s = \frac{x^2}{w^2} + \sin^2\frac{m\hat{\theta}}{2} \tag{2}$$

where

$$w \equiv 2\left|\frac{L_q A}{B_\theta}\right|^{1/2} \tag{3}$$

is the island *half*-width with $L_q \equiv q_s/q_s' \equiv r_s/\hat{s}$. Equation (2) yields an island topology, with "trapped" $(0 < s < 1)$ and "circulating" field lines $(0 < s < 1)$.

The procedure to obtain the island evolution equation is standard [20] and will only be sketched here. Using Ohm's law, $\nabla\cdot\mathbf{J} = 0$ for the current density, and $\boldsymbol{z}\cdot\mathbf{J} \equiv J = \nabla^2\psi$ one then obtains

$$\nabla^2 A \cos m\hat{\theta} = \frac{1}{\eta}\frac{\partial A}{\partial t}\left\langle \cos m\hat{\theta}\right\rangle + J_0'\left(\langle x\rangle - x\right). \tag{4}$$

Here,

$$\langle\bullet\rangle \equiv \oint_s d\hat{\theta}\left(\frac{\partial s}{\partial x}\right)^{-1}\bullet \Big/ \oint_s d\hat{\theta}\left(\frac{\partial s}{\partial x}\right)^{-1}$$

is an averaging procedure which annihilates the electrostatic potential in Ohm's law, and η is the resistivity along the strong B_z component of the magnetic field.

The last term, which is proportional to the equilibrium current gradient has been generally omitted [20,21,2,22–24,4]. Its importance can however readily be verified by taking the large x limit of (4)

$$\frac{\partial^2 A}{\partial x^2}\cos m\hat{\theta} = \mathcal{O}(A^2) + \frac{\lambda_s}{r_s x} A\cos m\hat{\theta}, \tag{5}$$

where

$$\lambda_s = -\frac{r_s q_s J'(r_s)}{q'(r_s)B_\theta}. \tag{6}$$

and noting that the linearized version of (5) produces the singularity at $x = 0$. Without this singularity, there could be no asymptotic matching procedure.

The equation describing the temporal evolution of the island width is derived by applying $\frac{1}{\pi A}\int_{-\infty}^{\infty} dx \int_{-\pi}^{\pi} d\theta \cos m\hat{\theta}$ onto (4). Expanding $A = A_0 + A'_{\pm}x + \cdots$ where $+$ stands for $x > 0$ and $-$ denotes $x < 0$, one finds that the A_0 term only contributes to the first two terms of (4), which yield the Rutherford equation [20]. Upon using the approximation

$$x = \pm w\left(s - \sin^2\frac{m\hat{\theta}}{2}\right)^{1/2} + \frac{w^2}{4}\frac{A'_{\pm}}{A_0}\cos m\hat{\theta} + \cdots$$

one then gets,

$$\frac{A'_+ - A'_-}{A_0} = \frac{2k\tau_R}{r_s}\frac{d}{dt}\left(\frac{w}{r_s}\right) - k\lambda_s\frac{A'_+ + A'_-}{A_0}w \tag{7}$$

where $k \approx 0.83$, and $\tau_R \equiv r_s^2/\eta$ the resistive time scale. The first term of (7) gives the well-known Δ' parameter and the last the matching index of ballooning parity. These matching data are provided from the outer region where the solution can be written [25]

$$\frac{A_{outer}}{A_0} = \left|\frac{x}{r_s}\right|^{\frac{1}{2}-\mu}\left(1+\frac{\lambda_s}{1-2\mu}x+\cdots\right)+\frac{\Delta'}{2}\left|\frac{x}{r_s}\right|^{\frac{1}{2}+\mu}(1+\cdots)+\frac{\Gamma'}{2}\left|\frac{x}{r_s}\right|^{\frac{1}{2}+\mu}\mathrm{sgn}x\,(1+\cdots) \tag{8}$$

as $x \to 0$. The first term in (8) represents the large solution, which is assumed here to be of even parity to leading order. The remaining two terms are the small solutions of even (odd) parity with leading coefficients $\Delta'/2$ ($\Gamma'/2$). In (8), μ is given by the equilibrium and can be shown to be equal to $\sqrt{-D_I}$ where D_I is the Mercier stability index against ideal localized modes. In the $\beta \to 0$ limit we have $\mu \to \frac{1}{2}$. This is also the limit where the next order terms in the large solution (8) become singular so that, in order to get a finite solution, Γ' must also become infinite. Assuming for the moment $\mu - \frac{1}{2}$ to be small but not zero, we proceed and find

$$\frac{A'_+ + A'_-}{A_0} \to \tilde{\Gamma}' + 2\lambda_s \ln\left|\frac{w}{r_s}\right| + \mathcal{O}(1-2\mu) \tag{9}$$

at distance $\pm w$, where

$$\tilde{\Gamma}' \equiv \Gamma' - \frac{\lambda_s}{\mu - \frac{1}{2}}$$

is the odd-parity renormalized index [26], which is well defined when $\beta \to 0$.

Substituting (9) in (7), the island width evolution equation thus becomes

$$r_s\Delta' = \frac{1.64\tau_R}{r_s}\frac{d}{dt}\frac{w}{r_s} - 1.64 r_s\lambda_s^2\left(\frac{w}{r_s}\right)\ln\left|\frac{w}{r_s}\right| - 0.83 r_s\lambda_s\tilde{\Gamma}'\left(\frac{w}{r_s}\right). \tag{10}$$

This equation is the main result of this section. It indicates that there is an effective matching index

$$\Delta(w) \equiv \Delta' + 1.64\lambda_s^2\left(\frac{w}{r_s}\right)\ln\left|\frac{w}{r_s}\right| + 0.83\lambda_s\tilde{\Gamma}'\left(\frac{w}{r_s}\right), \tag{11}$$

which includes finite island size effects. The index Δ' can be computed by solving the marginal stability equation in the outer, ideal region with the PEST-3 code [27], which

assumes $w \to 0$. The parameter λ_s is given by (6) and is a property of the unperturbed equilibrium at r_s. The last term is the quasi-linear stabilization obtained by White and Monticello [9], and Zakharov *et al.* [15].

One aspect that has been overlooked is that

$$\frac{A'_+ - A'_-}{A_0} \to (1-2\mu)\frac{r_s}{w} + \Delta' + \cdots$$

also produces an additional term at distance $\pm w$. This term represents a Glasser, Greene and Johnson stabilization [28] for the island evolution equation. A more rigorous approach [21] gives a pressure stabilization proportional to $3.1 D_R r_s/w$.

B. A current flattening model

It is shown in this section the current stabilization obtained previously as an inner layer effect is consistent with the correction in Δ' resulting from a flattening of the equilibrium profile in the outer region. Hence we are mainly concerned here with solving the marginal stability equation

$$\frac{1}{r}\frac{d}{dr}r\frac{d\Psi}{dr} - \frac{\lambda(r)}{r(r-r_s)}\Psi - \frac{m^2}{r^2}\Psi = 0 \tag{12}$$

for the perturbed radial magnetic field Ψ. Equation (12) is the Newcomb equation in the pressureless limit for a cylindrical plasma with circular cross-section. The boundary conditions are: Ψ must be regular as $r \to 0$ and vanish as $r \to \infty$. The function

$$\lambda(x) \equiv \frac{Rq_s J'(x)(x-1)}{B_z[q_s/q(x)-1]} \tag{13}$$

is proportional to the current gradient $J'(r)$ and give (6) at the rational surface position r_s, $x \equiv r/r_s$, B_z is the constant equilibrium magnetic field, R is the major radius and $q(r)$ the safety factor.

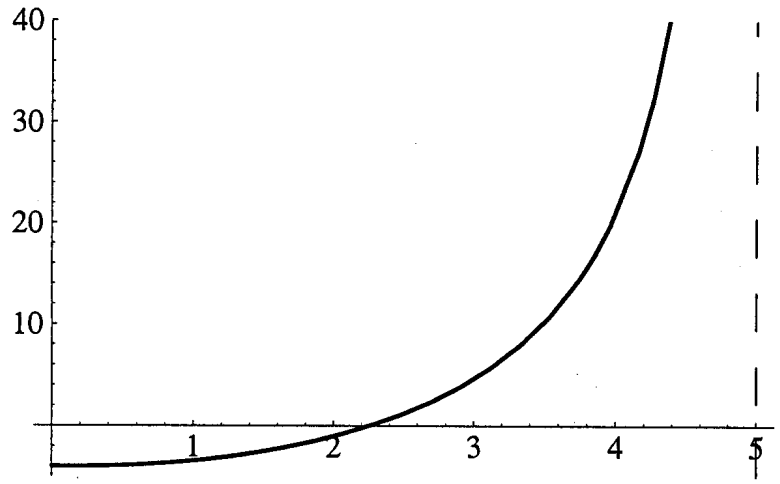

FIG. 3. Dependence of Δ' on the constant current gradient parameter $\lambda = \lambda_s$ for the $m = 2$ mode, which has a pole at $\lambda = 2m + 1 = 5$.

Exact solutions [29] exist in terms of the hypergeometric function $F(a, b, c|x)$ for $\lambda =$ const. Taking the wall at infinity, we then have

$$r_s\Delta_- = m - \frac{\lambda}{1+2m}\frac{F(1+a_-, 1+a_+, 2+2m|1-)}{F(a_-, a_+, 1+2m|1)}$$
$$r_s\Delta_+ = -m\nu - \frac{\lambda}{1+2m\nu}\frac{F(1+a_+, 1-a_-, 2+2m\nu|1-)}{F(a_+, -a_-, 1+2m\nu|1)}, \qquad (14)$$

where

$$r_s\Delta' \equiv r_s\Delta_+ - r_s\Delta_- \qquad \text{with} \qquad r_s\Delta_\pm \equiv \lim_{x\to 1\pm}\frac{d\Psi/dx}{\Psi}. \qquad (15)$$

Here, $a_\pm = m(1 \pm \nu)$ and $\nu \equiv \sqrt{1+\lambda/m^2}$. Equations (14) give the well-known result that $r_s\Delta' \to -2m$ in the large m limit ($\lambda/m \to 0$), and has a dependence in λ which is similar to the zero-β analytic formula $r_s\Delta' = -\pi\lambda\cot(\pi\lambda/2m)$ of Hegna and Callen [30]. One difference is that (14) yields a higher threshold for ideal instability: $\Delta' \to \infty$ as $\lambda \to 2m+1$ (see Fig. 3) whereas the marginal stability point given by Hegna and Callen is $2m$.

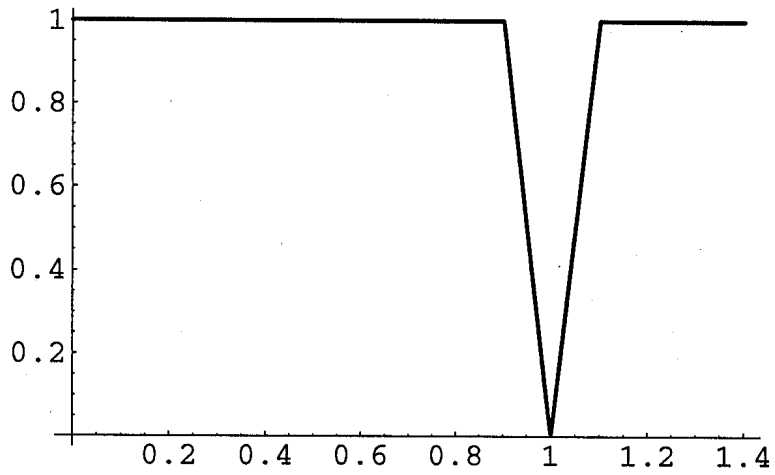

FIG. 4. Model for the current flattening: λ/λ_s vs. $x = r/r_s$ with $w = 0.1$.

To model the current flattening, we take $\lambda = \lambda_s|x-1|/w$ to vary linearly as shown in Fig. 4. This allows us to express the solutions as a linear combination of Bessel functions: $C_{21}\mathrm{J}_{2m}(2\sqrt{2\lambda_s(x-1)/w}) + C_{21}\mathrm{Y}_{2m}(2\sqrt{2\lambda_s(x-1)/w})$ where $1-w < x < 1$ and $C_{31}\mathrm{I}_{2m}(2\sqrt{2\lambda_s(x-1)/w}) + C_{32}\mathrm{K}_{2m}(2\sqrt{2\lambda_s(x-1)/w})$ where $1 < x < 1+w$. In total, there are six unknown coefficients which are determined by requiring the continuity of the solutions and their derivatives at $x = 1-w$ and $1+w$, and the continuity of Ψ at $x = 1$.

Figure 5 shows the effective reduction of Δ' as the flattening width w increases. The solid lines represent Δ' evaluated at $x \to 0\pm$ whereas the dashed lines correspond to $\Delta(w)$, that is Δ' computed at $1 \pm w$. Both definitions have the same $w \log w$ dependence, and to a large extent give the same stabilizing correction as w increases. One exception is for case (a) which has small $\lambda = 1$ and $\Delta' \approx -2m$. In this case the correction is slightly destabilizing with $\Delta(w) > \Delta'$.

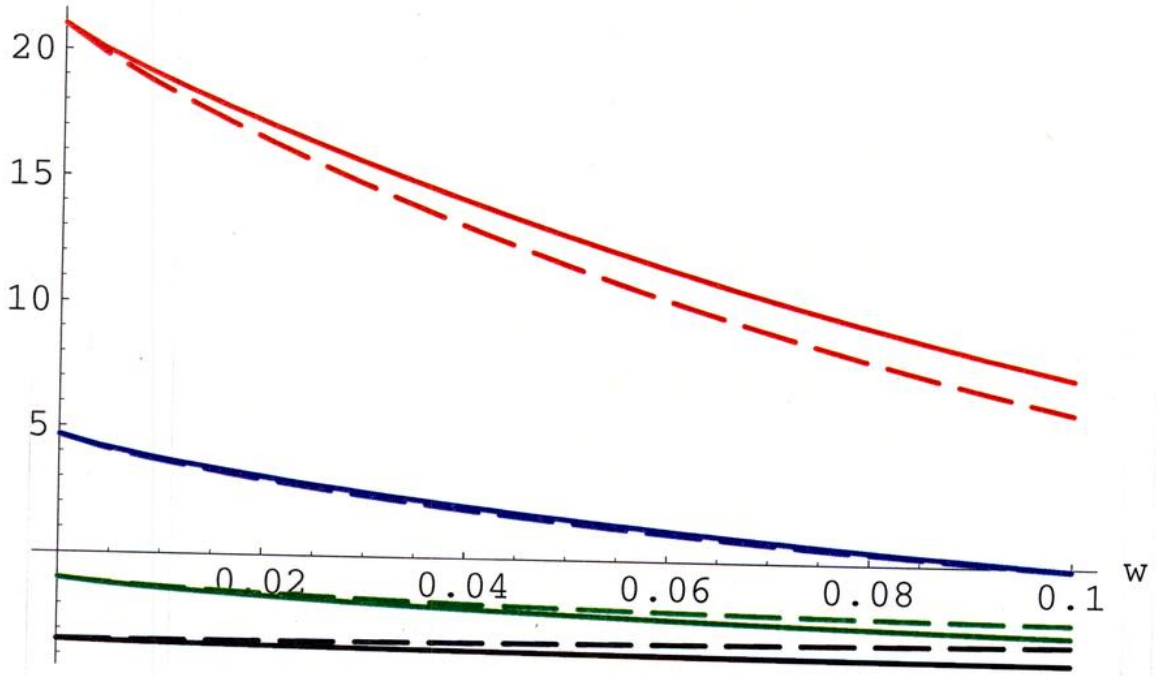

FIG. 5. The matching index Δ' and the effect of the current flattening over a half-width w for $\lambda_s = 1$, 2, 3 and 4 (Δ' increases with λ). The solid line corresponds to Δ' evaluated at $x = 1\pm$ whereas the dashed line is the index $\Delta(w)$ evaluated at $x = 1 \pm w$.

In Fig. 6, it is shown that the flattening correction has a dominant $2k\lambda_s^2 w \log w$ dependence and that the coefficient $2k$ is of the order of two over the range $0 < \lambda_s < 3.5$. This is in good agreement with the value $2k = 1.64$ found in § II A.

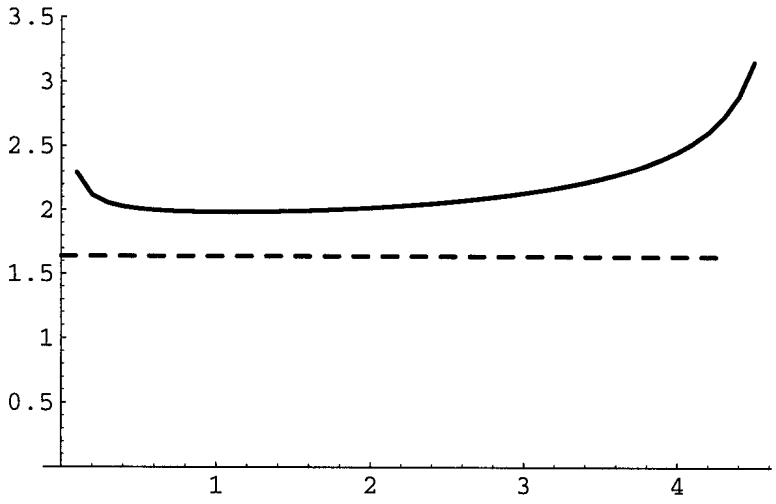

FIG. 6. Coefficient $2k$ vs. λ_s obtained by using a best fit of $\Delta'(w)$ to $\Delta'(0) + 2k\lambda_s^2 w \ln w + k_2 w$. The $2k = 1.64$ value obtained from the inner layer equation is shown in dashed line.

C. Application to an ITER equilibrium

The index Δ' is computed using PEST-3 for a low $\beta \approx 0.12\%$ toroidal equilibrium of ITER shape. The current density is gradually flattened over a distance $2w$ normalized to the square root of the poloidal flux coordinate about the the 3/2 and 2/1 surface, while keeping the safety factor value $q_0 = 1.05$ constant on axis. The $w \log w$ dependence is in this case also apparent for the 2/1 mode. There appears to be a small $1/w$ correction for the 3/2 mode that could be due to pressure effects.

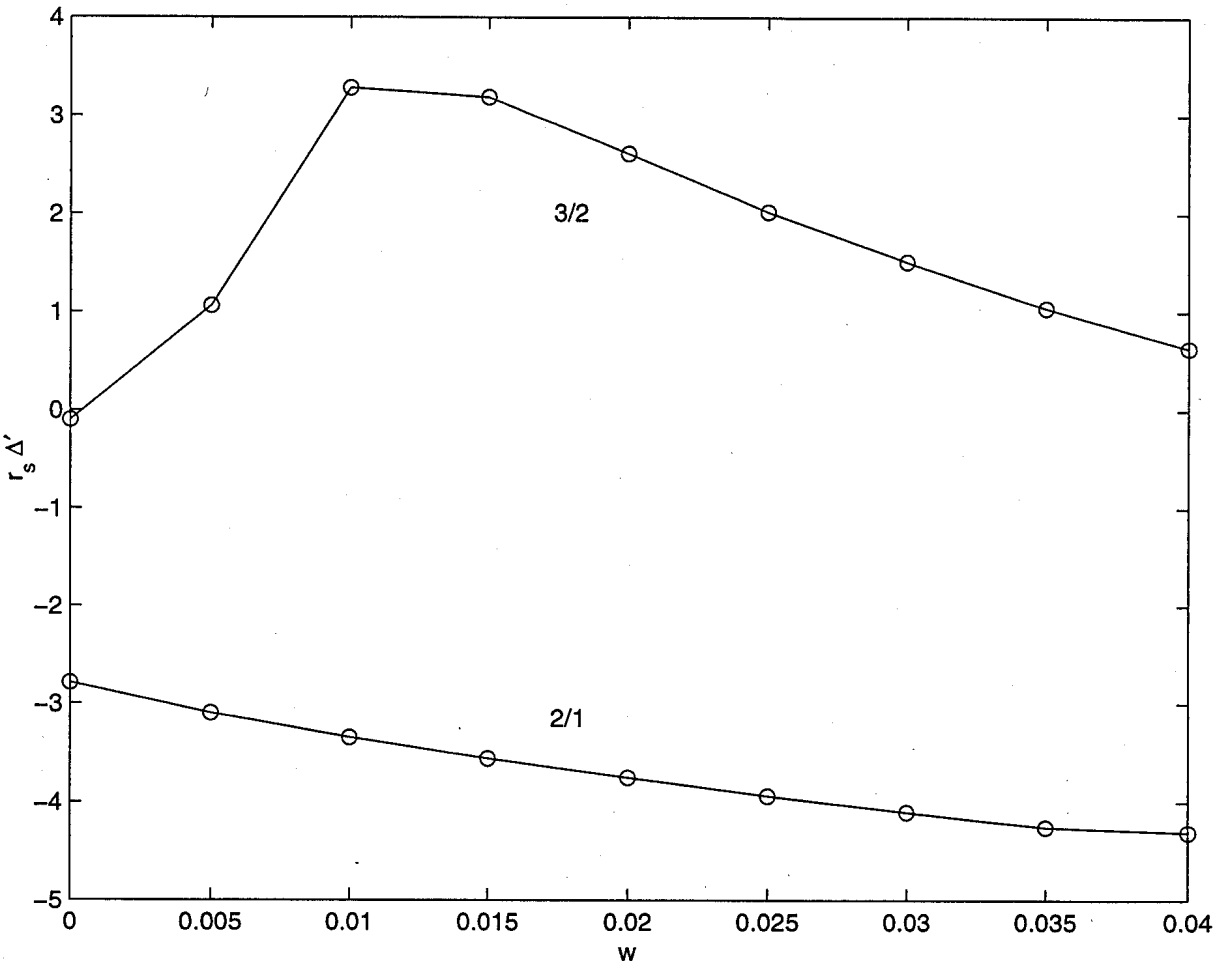

FIG. 7. The matching index Δ' vs. the half-width of the current density flattening width for the 2/1 and 3/2 modes.

III. STABILIZATION OF NEOCLASSICAL TEARING MODES USING A CONTINUOUS LOCALIZED CURRENT DRIVE

In ITER, the combination of weak Δ' with strong bootstrap current drive can yield large saturated islands. Figure 8 shows the Δ' matching data for various m/n resonant modes, $m = 2, 3, 4, 5, 6$ and $n = 1, 2, 3$. Higher m modes tend to be stable because $r_s\Delta' \to -2m$ as indicated by (14) and (15). Another factor of stabilization is the proximity of the rational surface to the conducting wall. It is found numerically and experimentally that the most dangerous modes are resonant at the 2/1, 3/2 and 4/3 surfaces. In the present case these three modes have a slightly negative Δ'.

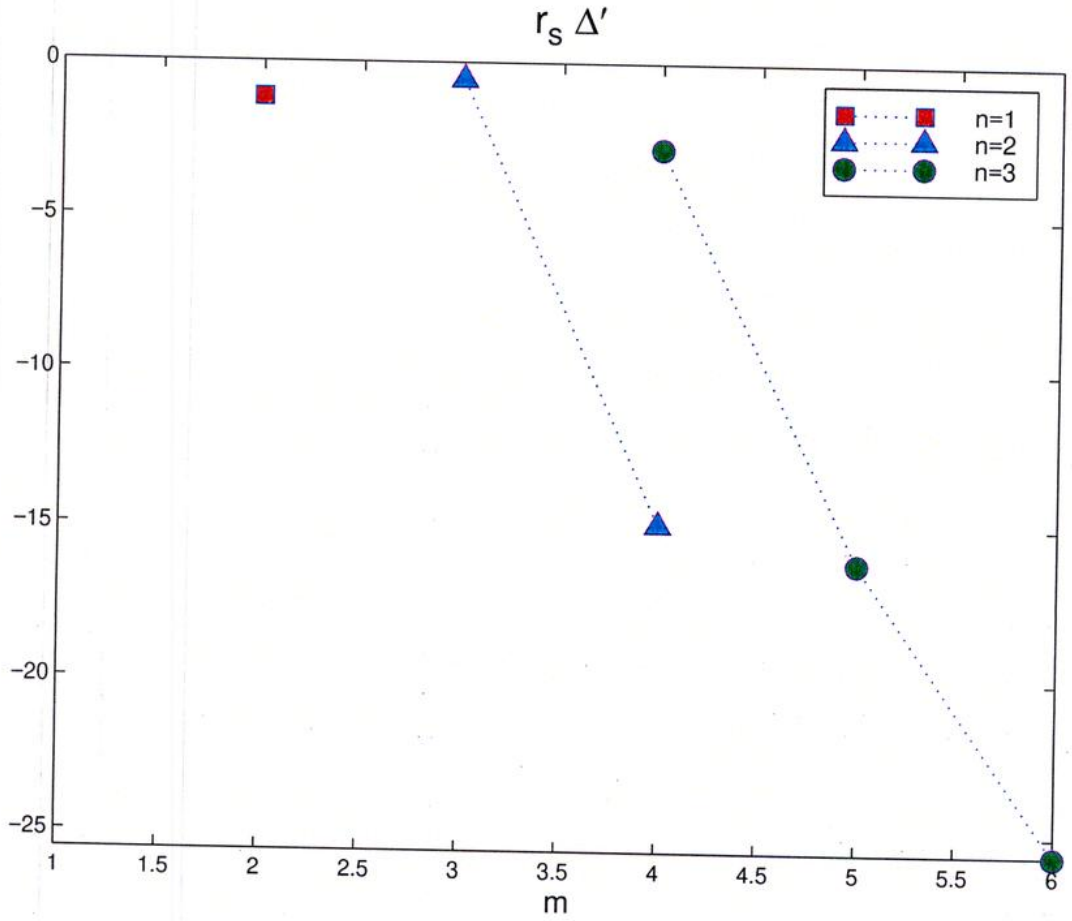

FIG. 8. The matching index Δ' is weakly stable for the 2/1, 3/2 and 4/3 modes.

Figure 9 is representative of the effect of strong bootstrap current drive combined with

moderate $r_s\Delta' = -2.6$. It shows the equilibrium helical flux

$$\psi_0 = \frac{1}{(2\pi)^2}\int d\tau \mathbf{B}_0\cdot\nabla\hat{\theta},$$

to which a helical perturbation $A\cos m\hat{\theta}$ has been added [c.f. (1)]. The radial behaviour of A is computed by solving the linearized outer region stability equation but with full toroidal effects. This means that A is known up to an arbitrary constant related to the island half-width (3), which is itself determined from the island equation

$$1.64\frac{\tau_R}{r_s}\frac{d}{dt}\left(\frac{w}{r_s}\right) = r_s\Delta(w) + 2.3\sqrt{\epsilon_s}\beta_p\frac{L_q}{L_p}\left(\frac{r_s}{w}\right) \tag{16}$$

and setting $d/dt = 0$. Here, we include the lowest order quasi-linear corrections as given by (11) with the Glasser, Greene and Johnson stabilization, i.e.

$$r_s\Delta(w) = r_s\Delta' + 3.1D_R\left(\frac{r_s}{w}\right) + 1.64\lambda_s^2\left(\frac{w}{r_s}\right)\ln\left|\frac{w}{r_s}\right|. \tag{17}$$

The third term in (16) represents the neoclassical bootstrap current drive [1–3], with $\epsilon_s = r_s/R$, $\beta_p = 2p/B_\theta^2$ and $L_q/L_p = -p'/q'$, all quantities being evaluated at the rational surface position. The polarization current and higher order quasi-linear corrections are neglected.

A. Effect of a Gaussian current at the rational surface on Δ'

Tearing modes can be made more stable by tailoring [31] the current profile in the vicinity of rational surfaces. Since stability depends on the gradient of the current density through the λ function defined in (13), small modifications in the current profile can have a substantial effect. It can be shown by inspection of (12) that $\lambda > 0$ is destabilizing for $r < r_s$ but stabilizing for $r > r_s$. Clearly, if the current gradient is made positive where $r < r_s$ and negative in the region where $r > r_s$, this can only be favourable to stability (i.e. Δ' decreases).

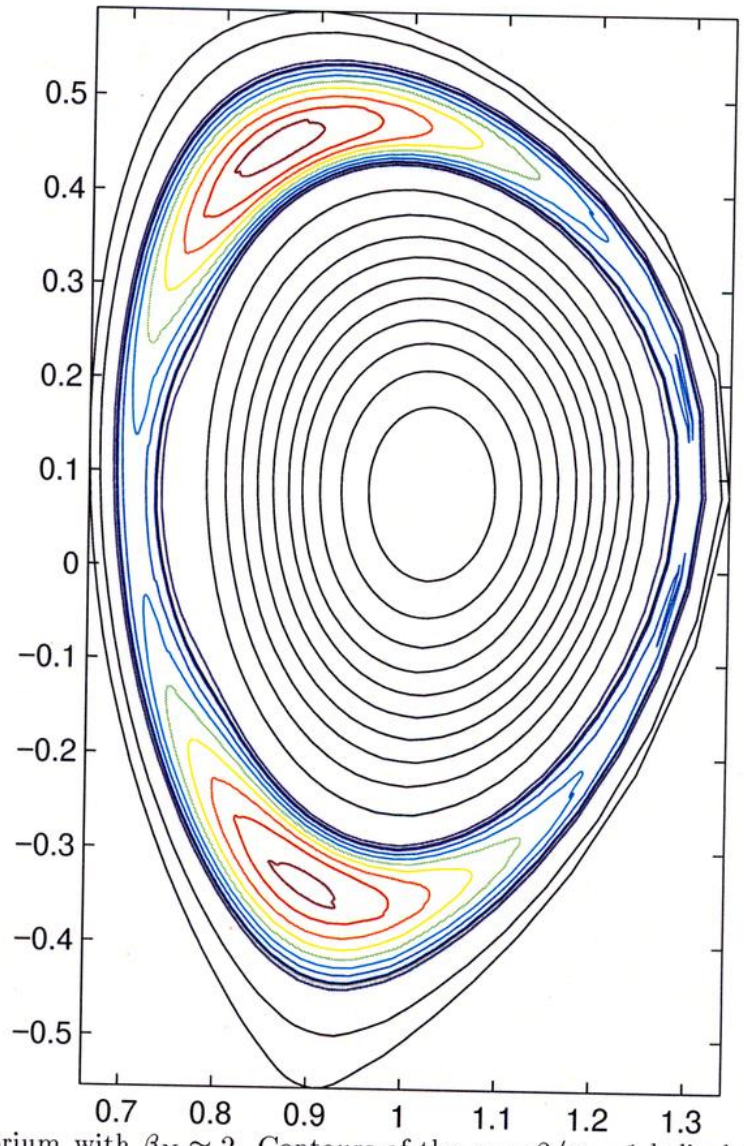

FIG. 9. ITER equilibrium with $\beta_N \approx 2$. Contours of the $m = 2/n = 1$ helical flux computed using the PEST-3 code. The island sits at $q = 2$ and $r_s\Delta' = -2.6$ in this case.

This is best seen by considering a specific example. Let us take a Gaussian current density profile,

$$J(x) = J_{CD} \exp\left[-\left(\frac{x}{\sigma} - \alpha\right)^2\right]$$

of radial extent σ, which peaks at $x = \alpha\sigma$ (x being the distance from the rational surface). For such a profile, (12) can be written approximately as

$$\psi''(x) \approx \frac{4}{\hat{s}\sigma}\left(\frac{J_{CD}}{J_q}\right)\frac{(x/\sigma - \alpha)\exp\left[-(x/\sigma - \alpha)^2\right]}{x}, \tag{18}$$

where $J_q \equiv 2B_z/Rq_s$ and $\hat{s} \equiv r_s q'/q$. Assuming the constant ψ approximation to hold, (18) can be integrated analytically, yielding

$$\Delta' \approx -\frac{4\sqrt{\pi}}{\hat{s}\sigma}\left(\frac{J_{CD}}{J_q}\right)[1 - w(\alpha)], \tag{19}$$

where

$$w(\alpha) = \frac{\alpha}{\sqrt{\pi}}\wp\int_{-\infty}^{\infty} dx \frac{\exp\left[-(x/\sigma - \alpha)^2\right]}{x} = -i\,\alpha\sqrt{\pi}\mathrm{erf}(i\alpha)\,\exp\left(-\alpha^2\right) \tag{20}$$

is shown in Fig. 10. In this approximation, the best results are achieved by aiming at the rational surface position ($\alpha = 0$) and taking a narrow channel width (σ small). The stabilization degrades, however, as $|\alpha|$ increases; when $|\alpha| > 1$, Δ' becomes positive and reaches a maximum at $\alpha \approx 1.6$. At this point, the Gaussian bump sits on either side of the rational surface and the stabilizing effect is lost.

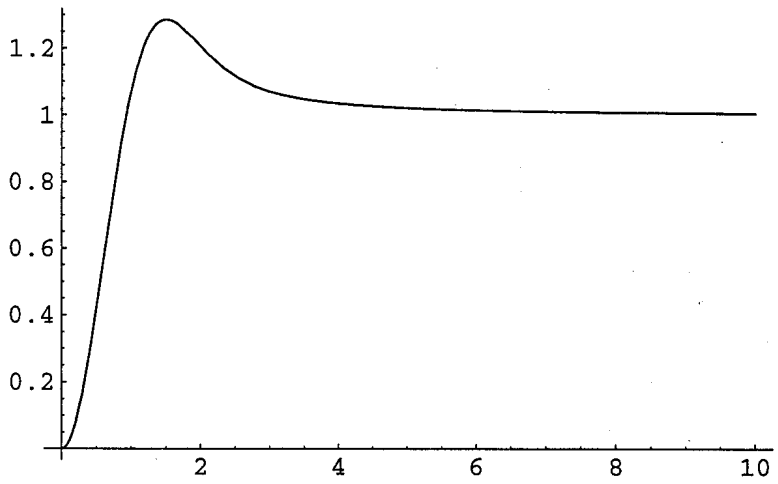

FIG. 10. Function $w(\alpha)$ representing the stabilization/destabilization factor. The Gaussian current density is stabilizing for $w(\alpha) < 1$ but destabilizing for $w(\alpha) > 1$.

Equation (19) can be regarded as a correction to Δ' when a Gaussian current distribution is added to the equilibrium current if J_{CD} and σ are small. One effect not taken into account

is the flattening of the safety factor profile due to the addition of the Gaussian current. A more realistic model consists of a current distribution to which a Gaussian perturbation is added with safety factor and current profiles computed self-consistently, as in Fig. 11. The black curve is the response to the unperturbed equilibrium current density. The stabilizing effect of the incremental Gaussian current is clearly noticeable from the jump in derivatives at the rational surface. Here we observe that the stabilization is more effective when applying the Gaussian current outward with respect to the unperturbed rational surface position, a direct consequence of the the rational surface moving toward the edge as J_{CD} increases. Note that the current drive effectively adds an odd contribution to λ, which is negative inside and positive outside the rational surface.

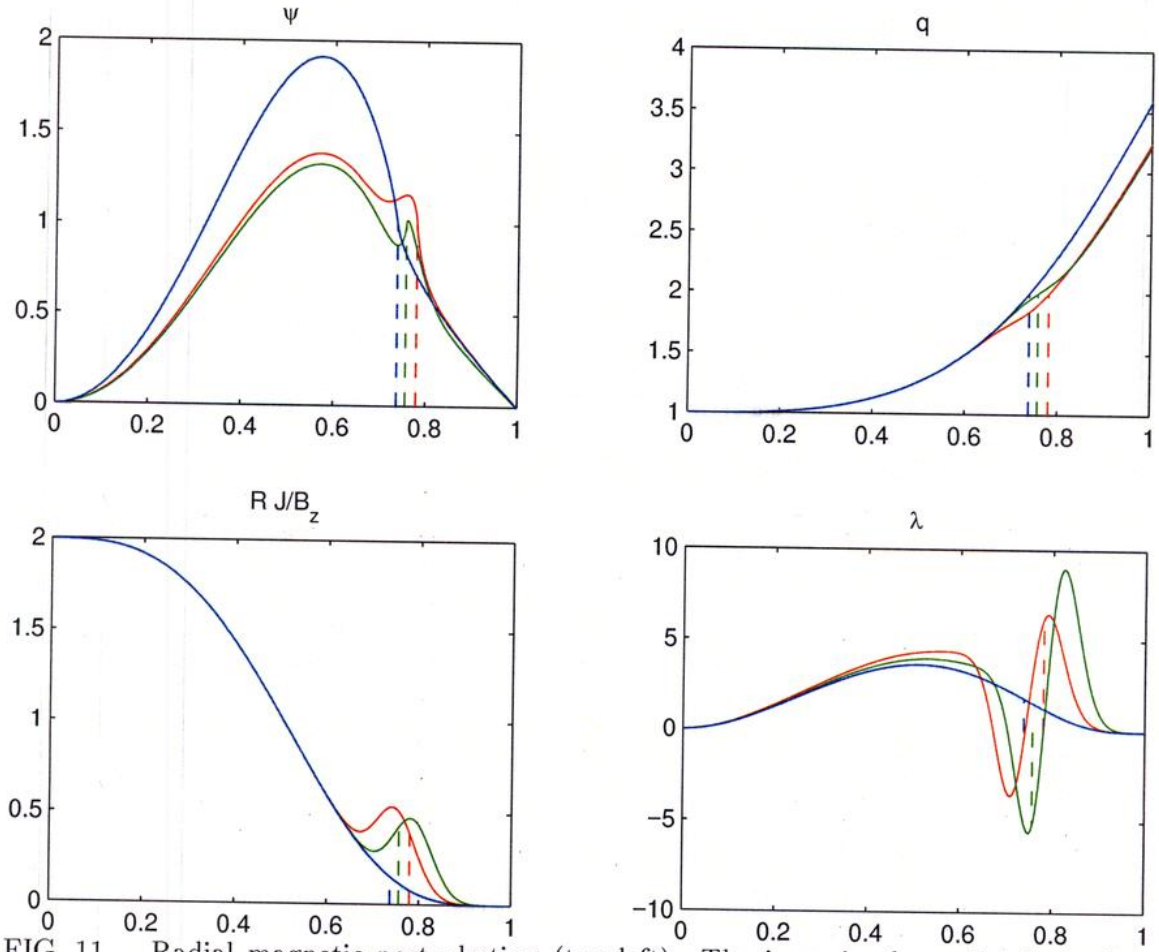

FIG. 11. Radial magnetic perturbation (top left). The jump in the radial derivative takes place at the rational surface position, whose position is indicated by a vertical dashed line. The black curves correspond to the unperturbed equilibrium.

B. ECCD at the $q = 2/1$ surface in ITER

The code PEST-3 has been used to determine Δ' for an ITER profile, as predicted immediately after a sawtooth crash. A convergence study has been performed to estimate Δ' by gradually increasing the number of mesh nodes, and extrapolating to infinity. The current profile is characterized by a significant bootstrap current component at the 2/1 rational surface, which amounts to 11% of the current on axis ($\beta_N = 1.9$). The result of adding the ECCD is shown in Fig. 12. The curves correspond to $\sigma = 0.03$ (peaked Gaussian), $\sigma = 0.06$ and $\sigma = 0.12$ (broad Gaussian). The ECCD is applied inside at $\alpha = -0.5$, at the unperturbed rational surface position $\alpha = 0$ and outside at $\alpha = 0.5$. In addition, the current density J_{CD} is varied from zero to $\sim 30\%$ of the current density on axis. The total current in the Gaussian ECCD amounts to 5 % of the toroidal current for the peaked ECCD, and 30 % of the plasma current for the broad ECCD.

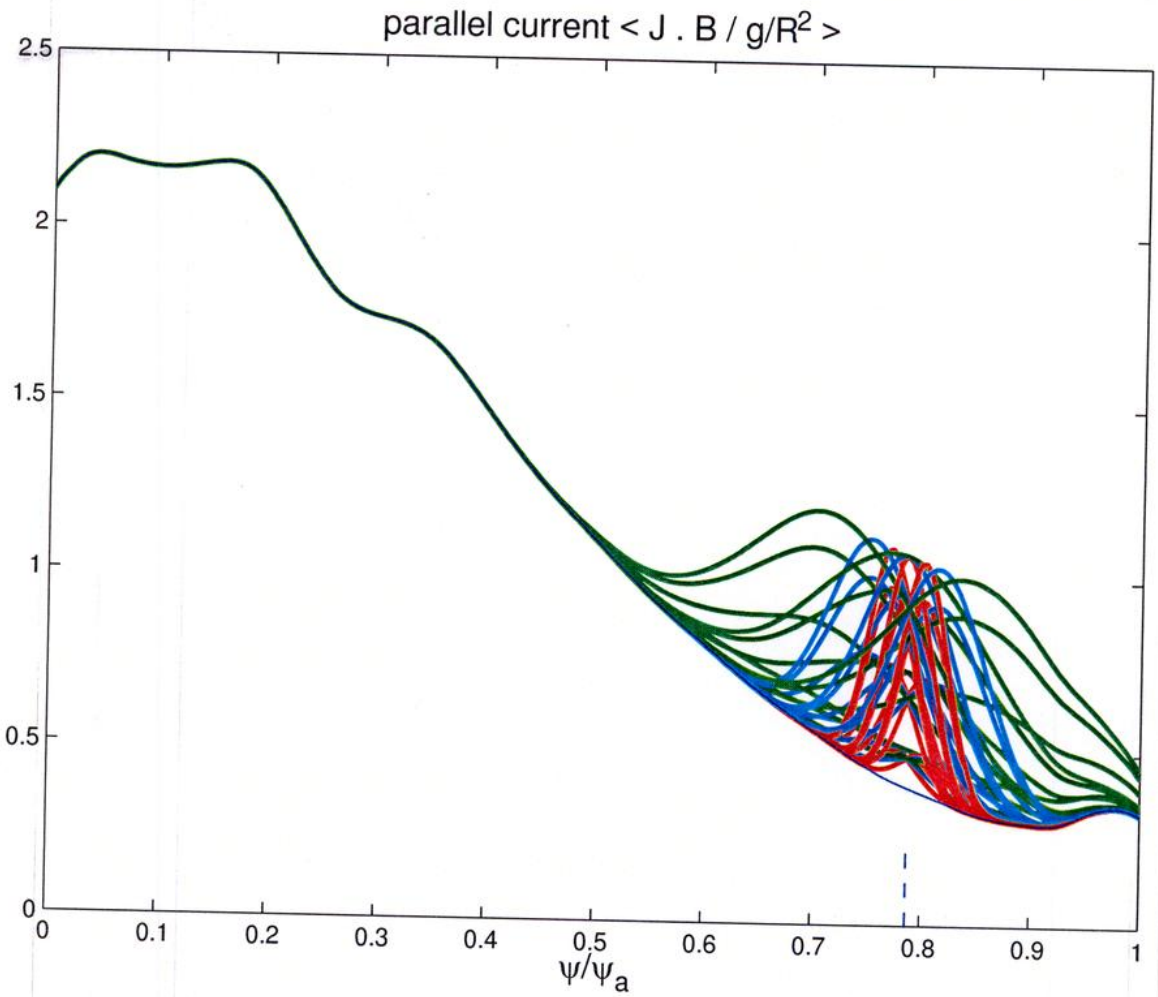

FIG. 12. Parallel current with ECCD channel about the rational surface.

The numerical results confirm our earlier predictions that the stabilization is inversely proportional to J_{CD} over the channel width σ, or $\propto I_{CD}/\sigma^2$. The effectiveness of the stabilization of the ECCD is rapidly lost, however, when applied inside (triangles pointing to the left). This is due to the rational surface that shifts outwards with J_{CD} to the point where α becomes larger than one. Our theory then predicts a destabilization. In the worst scenario, this destabilization can reach 30 % [$\approx (w_{max} - 1)/(1 - w_{min})$] of the maximum attainable stabilization in Δ' at $\alpha = 0$, in agreement with Fig. 10. Applying the ECCD at $\alpha = 0$ (diamonds) gives the most negative Δ' at low I_{CD} but becomes destabilizing at larger I_{CD}. The most robust stabilization is for $\alpha = 0.5$ (triangles pointing to the right).

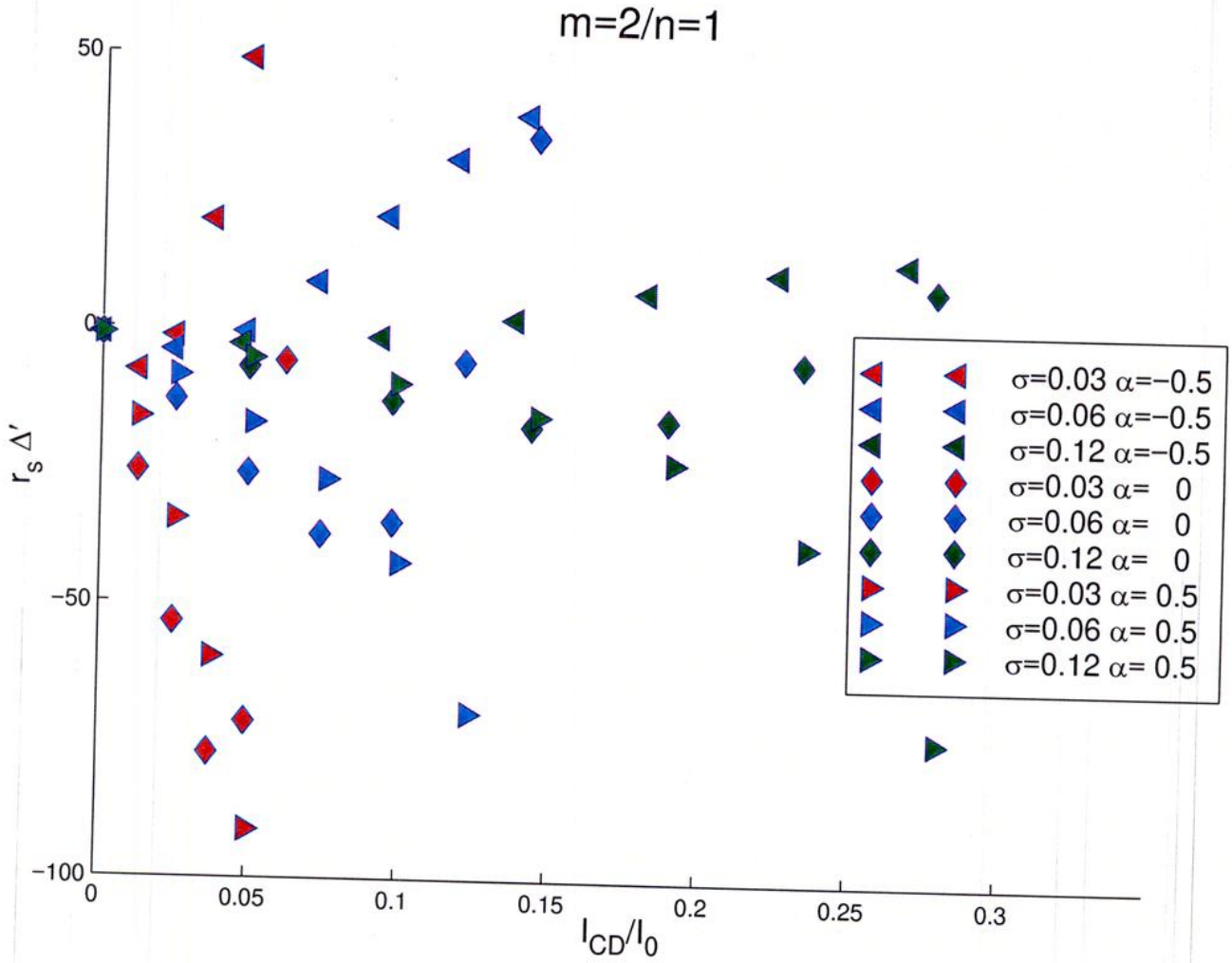

FIG. 13. ECCD stabilization is more effective when applying just outside the rational surface.

The effect of an ECCD at the 2/1 surface is also investigated on the neighbouring rational surfaces. With the exception of the cases where the ECCD overlaps these rational surfaces, the ECCD is slightly destabilizing, as expected. For any parameter choice, however, the 5/2 surface remains stable, whereas there is a large parameter range for the 3/2 surface where this destabilization remains modest. The choice of $\alpha \approx 0.5$ combined with $0.5 < \sigma < 0.1$ and $I_{CD}/I_0 \approx 0.05$, for instance, reduces Δ' at the 2/1 surface to -20 while barely affecting the stability at the 3/2 surface.

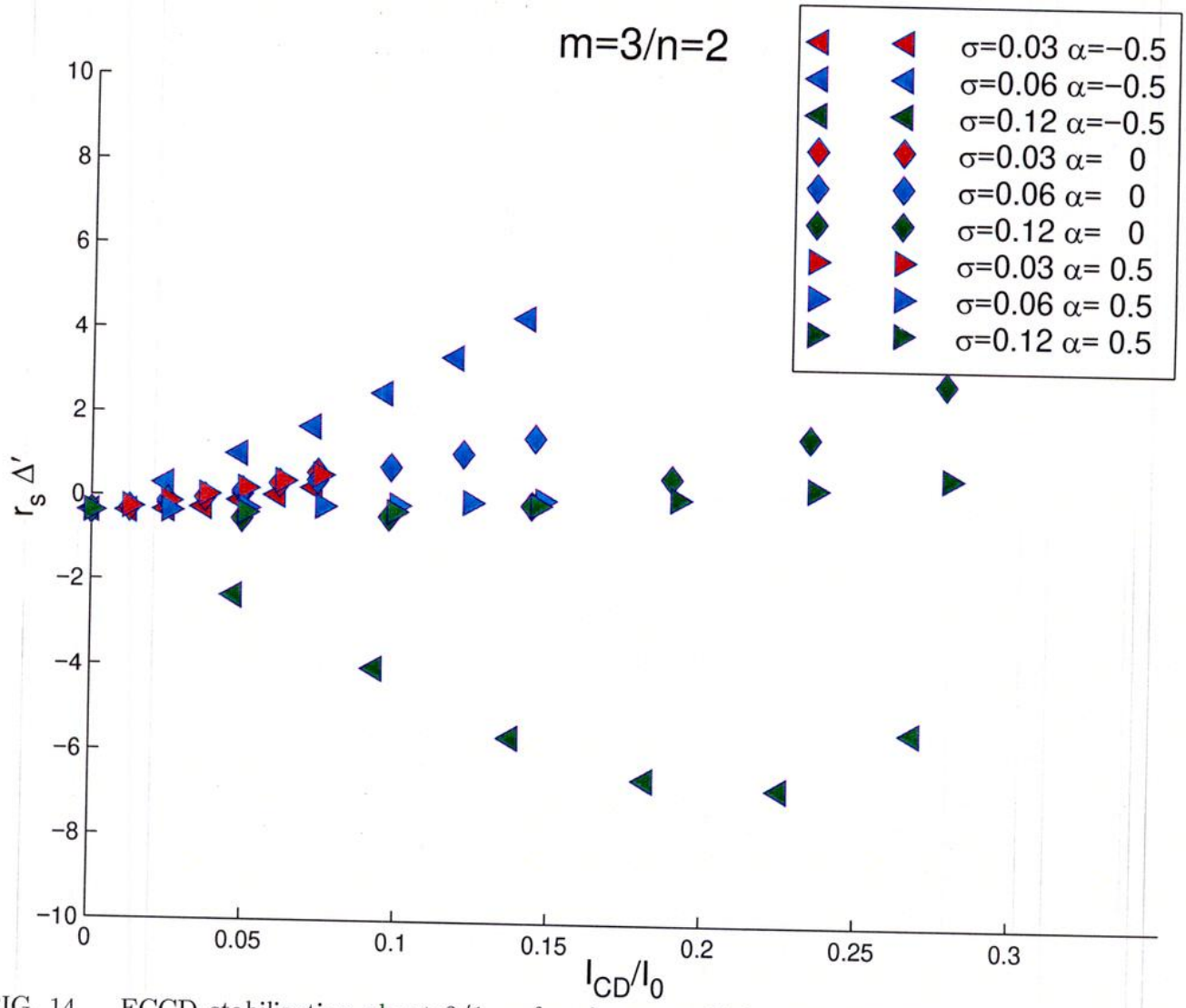

FIG. 14. ECCD stabilization about 2/1 surface has a small destabilizing influence on 3/2 surface.

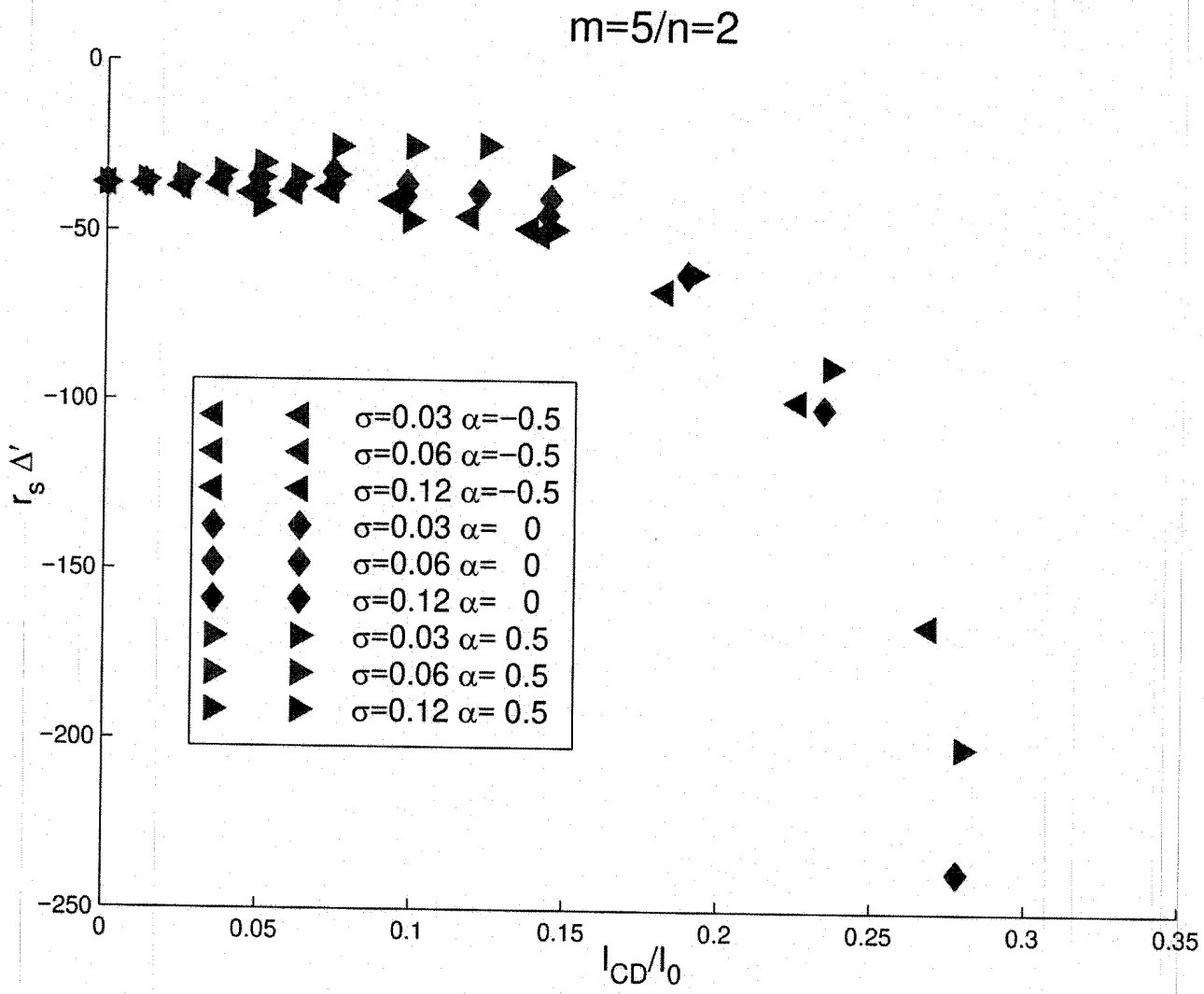

FIG. 15. ECCD stabilization about 2/1 surface cannot destabilize the 5/2 mode.

IV. RESISTIVE WALL BOUNDARY CONDITIONS

A. Geometry

Adopting a cylindrical (r, ϕ, z) coordinate system, we assume the existence of a plasma surrounded by a closed, toroidally symmetric wall with finite resistivity as shown in Figs. 16 and 17. Apart from a finite set of vertical field coils and a toroidally symmetric toroidal field coil, we have a "vacuum" region, which extends from the wall to infinity. The volume inside the wall will be referred to as the plasma or *interior* region. The tangential conductivity σ of the wall will be assumed to be sufficiently large so that the product of σ times the wall thickness δ is finite.

The geometry of the wall in the poloidal plane is parametrized by the angle θ,

$$\left.\begin{aligned} r &= r(\theta) \\ z &= z(\theta) \end{aligned}\right\} \tag{21}$$

which increases by 2π after performing one poloidal turn in the counterclockwise direction. The normal gradient to the wall surface then reads

$$\frac{\partial}{\partial n} = \mathbf{n}\cdot\boldsymbol{\nabla} = \frac{1}{\rho_\theta}\left(z_\theta \frac{\partial}{\partial r} - r_\theta \frac{\partial}{\partial z}\right) \equiv \frac{1}{\rho_\theta}\frac{\partial}{\partial u},$$

where

$$\rho_\theta \equiv \sqrt{r_\theta^2 + z_\theta^2}$$

and the subscript θ denotes ∂_θ.

B. Magnetic field representation

In the vacuum region, the magnetic field $\mathbf{B}$ satisfies

$$\boldsymbol{\nabla}\cdot\mathbf{B} = 0 \tag{22}$$

$$\boldsymbol{\nabla}\times\mathbf{B} = \sum_i \mathbf{J}_i \tag{23}$$

where $\mathbf{J}_i = I_i\,\delta(r - r_i)\delta(z - z_i)\hat{\phi}$, $i = 1, \cdots N_i$ are toroidally symmetric current filaments which model the vertical field coils.

For convenience, $\mathbf{B}$ is split into

$$\mathbf{B} = \mathbf{B}_J + \mathbf{B}_w, \tag{24}$$

where $\mathbf{B}_J$ is driven by the $\mathbf{J}_i$ currents and $\mathbf{B}_w$ is the remaining contribution which arises from the presence of the wall.

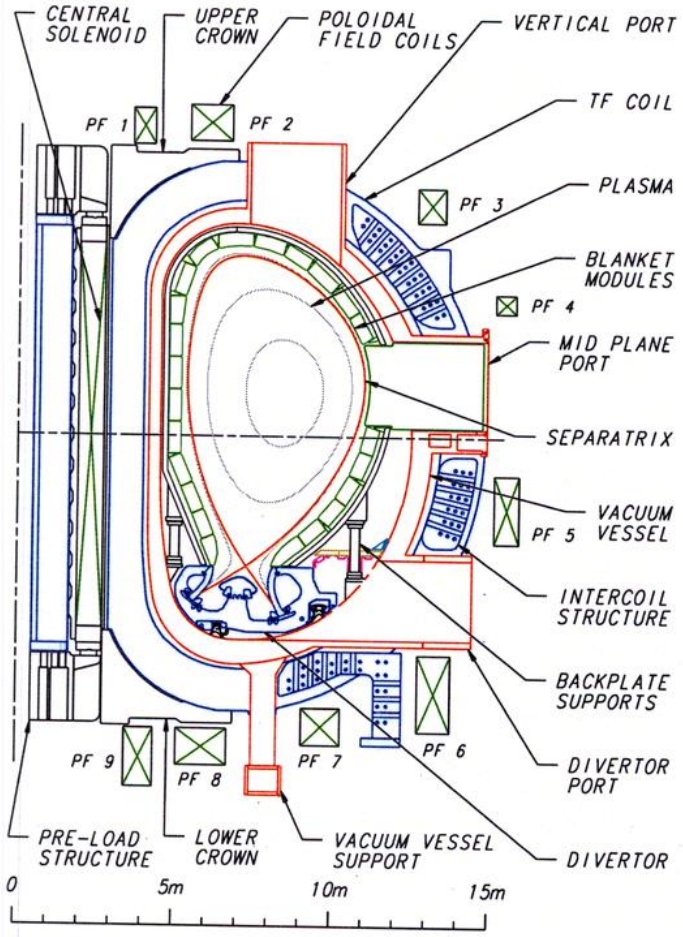

FIG. 16. Poloidal cross section of the ITER tokamak showing the geometry of the conducting wall and the disposition of the external vertical field coils (PF coils).

1. Field from the external coils

The contribution $\mathbf{B}_J$ driven by the $\mathbf{J}_i$'s is best resolved by expressing

$$\mathbf{B}_J = \boldsymbol{\nabla}\times\mathbf{A}_J \tag{25}$$

which satisfies (22), and rewriting (23) as

$$\boldsymbol{\nabla}\times\boldsymbol{\nabla}\times\mathbf{A}_J = \sum_i \mathbf{J}_i. \tag{26}$$

Due to toroidal geometry and the fact that $\mathbf{J}$ is parallel to $\hat{\phi}$, only the covariant component $\mathbf{A} = \psi\boldsymbol{\nabla}\phi$ survives and satisfies

$$\boldsymbol{\nabla}\cdot\frac{1}{r^2}\,\boldsymbol{\nabla}\psi = -\sum_i J_i^{\phi}, \tag{27}$$

where $J_i^{\phi} = \mathbf{J}_i\cdot\boldsymbol{\nabla}\phi$ is the contravariant component. This equation is solved using the Green's function technique,

$$\psi = \frac{r}{4\pi}\sum_i I_i\,\bar{G}(\boldsymbol{\rho},\boldsymbol{\rho}_i) \tag{28}$$

where $\bar{G}(\boldsymbol{\rho},\boldsymbol{\rho}_i)$ is the two-dimensional Green's function satisfying

$$r\,\boldsymbol{\nabla}\cdot\frac{1}{r^2}\,\boldsymbol{\nabla}r\,\bar{G}(\boldsymbol{\rho}',\boldsymbol{\rho}) = -4\pi\delta(\boldsymbol{\rho}'-\boldsymbol{\rho}) \tag{29}$$

and $\boldsymbol{\rho} = (r,z)$. For the Grad-Shafranov equation, the Green's function is

$$\bar{G}(\boldsymbol{\rho}',\boldsymbol{\rho}) = 2\pi r G_1(\boldsymbol{\rho}',\boldsymbol{\rho}) \tag{30}$$

where G_1 is the $n=1$ Green's function of § IV B 5, that is

$$\bar{G}(\boldsymbol{\rho}',\boldsymbol{\rho}) = \pi\left(\frac{r}{r'}\right)^{\frac{1}{2}} p^{\frac{3}{4}} F(\tfrac{3}{2},\tfrac{1}{2},2|p) \tag{31}$$

where

$$r' \equiv r(\theta'), \quad z' \equiv z(\theta') \quad p \equiv \frac{s-1}{s+1}, \quad s \equiv \frac{\lambda}{\sqrt{\lambda^2-1}}, \tag{32}$$

$$\lambda \equiv \frac{r'^2 + r^2 + (z'-z)^2}{2r'r} = 1 + \frac{(r'-r)^2 + (z'-z)^2}{2r'r} = 1 + \frac{|\boldsymbol{\rho}' - \boldsymbol{\rho}|^2}{2r'r}, \tag{33}$$

and

$$F(a,b,c|x) = 1 + \frac{ab}{c}x + \frac{a(a+1)b(b+1)}{c(c+1)}\frac{x^2}{2!} + \cdots \tag{34}$$

is Gauss' hypergeometric series.

2. Field contribution from the wall

The magnetic field originating from the wall is irrotational and can thus be written [32] as

$$\mathbf{B}_w = \boldsymbol{\nabla}\chi^* \tag{35}$$

with

$$\boldsymbol{\nabla}^2\chi^* = 0. \tag{36}$$

It is however well-known [33] that when the (vacuum) domain is multi-connected [34] χ^* is not single-valued. Choosing a contour of integration around a poloidal cross-section of the plasma [see Fig. 17],

$$\oint_{C_a} d\mathbf{l}\cdot\mathbf{B}_w = \oint_{C_a} d\mathbf{l}\cdot\boldsymbol{\nabla}\chi^* = \chi^*|_{\theta=2\pi} - \chi^*|_{\theta=0} = I_a, \tag{37}$$

we find that χ^* has a branch cut; the jump of χ^* across the discontinuity amounting to the sum of the toroidal current I_a flowing in the plasma and in the wall. Likewise, if we choose our integration contour along the ϕ direction so as to intersect the current I_b flowing in the toroidal field coils, we get

$$\oint_{C_b} d\mathbf{l}\cdot\boldsymbol{\nabla}\chi^* = \chi^*|_{\phi=2\pi} - \chi^*|_{\phi=0} = I_b. \tag{38}$$

The multi-valued character of χ^* can however be easily accommodated provided we write

$$\chi^* = \chi + k_a\ \theta + k_b\ \phi \tag{39}$$

where χ is single-valued and satisfies,

$$\nabla^2\chi = 0, \tag{40}$$

with

$$k_{a,b} = \oint_{C_{a,b}} d\mathbf{l}\cdot\mathbf{B}/2\pi \tag{41}$$

being constants that can be determined from the toroidally symmetric $\mathbf{B}$ in the plasma.

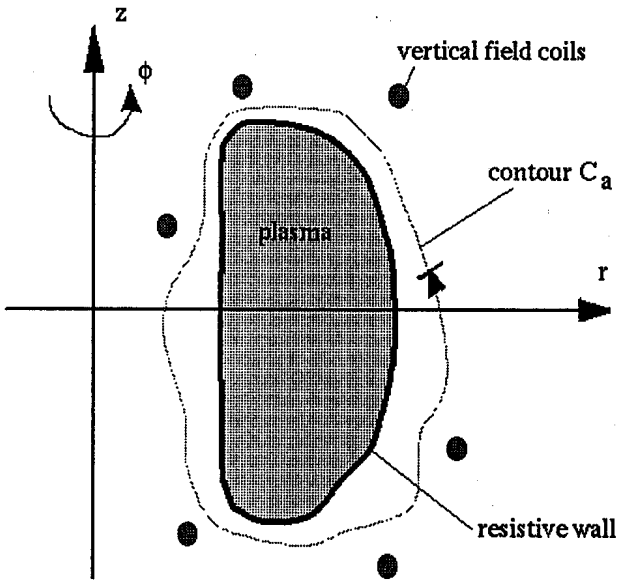

FIG. 17. Schematic cross-section of the poloidal plane. The plasma is surrounded by a closed and toroidally symmetric wall. There are a finite number of vertical field coils in the vacuum region (the toroidal field coils are not shown). The contour C_a circumscribes the plasma but excludes the vertical field coils.

3. Green's function solution for χ

The scalar potential χ can be obtained at any point in space using Green's theorem

$$\left.\begin{array}{r} -4\pi\chi(\mathbf{x}') \\ -2\pi\chi(\mathbf{x}') \\ 0 \end{array}\right\} = \int_\Sigma d\boldsymbol{\sigma}\cdot\{G(\mathbf{x}',\mathbf{x})\nabla\chi(\mathbf{x}) - \nabla G(\mathbf{x}',\mathbf{x})\chi(\mathbf{x})\}, \tag{42}$$

where Σ is any closed surface and

$$G(\mathbf{x}', \mathbf{x}) = \frac{1}{|\mathbf{x}' - \mathbf{x}|}$$

is the three-dimensional Green's function for the Laplacian operator, i.e. $\nabla^2 G(\mathbf{x}', \mathbf{x}) = -4\pi\delta(\mathbf{x}' - \mathbf{x})$. Here, the enclosed volume extends from ∞ to Σ and the value of the left-hand side of (42) depends on whether $\mathbf{x}'$ is inside the enclosed volume, lies on the surface Σ, or is outside the volume, respectively.

Upon writing

$$d\boldsymbol{\sigma}\cdot\nabla = r\frac{\partial}{\partial u}$$

and expanding

$$\chi(\mathbf{x}) = \sum_{n=-\infty}^{\infty} \chi_n(\boldsymbol{\rho}) \exp in\phi \tag{43}$$

$$G(\mathbf{x}', \mathbf{x}) = \sum_{n=-\infty}^{\infty} G_n(\boldsymbol{\rho}', \boldsymbol{\rho}) \exp in(\phi' - \phi) \tag{44}$$

in toroidal Fourier modes, (42) then reduces to

$$\int_0^{2\pi} d\theta \left\{ r\, G_n(\boldsymbol{\rho}', \boldsymbol{\rho})\, \frac{\partial \chi_n}{\partial u}(\boldsymbol{\rho}) + [\delta(\theta' - \theta) - r\, K_n(\boldsymbol{\rho}', \boldsymbol{\rho})]\, \chi_n(\rho) \right\} = 0, \tag{45}$$

where

$$K_n \equiv \frac{\partial G_n}{\partial u}. \tag{46}$$

4. Finite element discretization

In virtue of the toroidal symmetry of the wall, (45) can be solved independently for every toroidal mode n. Dropping the subscript n from now on, we further expand

$$\left.\begin{aligned} \chi &= \textstyle\sum_i \chi_i\, e_i(\theta) \\ \partial_u \chi &= \textstyle\sum_i \zeta_i\, e_i(\theta) \end{aligned}\right\} \tag{47}$$

in piecewise constant finite elements e_i. Equation (45) then becomes the system

$$\chi_i = \sum_j V_{ij}\, \zeta_j \tag{48}$$

where

$$V_{ij} \equiv -\sum_k (B_{ik})^{-1} A_{kj}, \tag{49}$$

$$A_{ij} \equiv \int_0^{2\pi} d\theta\; r\; G(\theta_i, \theta)\; e_j(\theta) \tag{50}$$

and

$$B_{ij} \equiv \int_0^{2\pi} d\theta\; [\delta(\theta_i - \theta) - \; r\; K(\theta_i, \theta)]\; e_j(\theta). \tag{51}$$

5. Expressions for G and K

The Fourier projection

$$\begin{aligned} G(\boldsymbol{\rho}', \boldsymbol{\rho}) &= \frac{1}{2\pi} \int_0^{2\pi} d\phi' \exp\left[-in(\phi' - \phi)\right] G(\mathbf{x}', \mathbf{x}) \\ &= \frac{1}{2\pi} \int_0^{2\pi} d\phi' \frac{\cos n(\phi' - \phi)}{[r'^2 + r^2 - 2r'r\cos(\phi' - \phi) + (z' - z)^2]^{\frac{1}{2}}} \\ &= \left(\frac{1}{\pi r' r}\right)^{\frac{1}{2}} \Gamma(\tfrac{1}{2} + n)\; p^{\frac{n}{2} + \frac{1}{4}}\; \frac{F\left(n + \frac{1}{2}, \frac{1}{2}, n + 1 | p\right)}{\Gamma(n+1)} \end{aligned} \tag{52}$$

can be obtained analytically, with λ, s and p defined in (32) and (33). Since $\lambda \geq 1$ we have $1 \leq s < \infty$ and $0 < p < 1$. The hypergeometric function $F\left(n + \frac{1}{2}, \frac{1}{2}, n + 1 | p\right)$ is evaluated in the WALL code using the freeware routine "hyp2f1" of the Cephes Math Library, which has proved to be very accurate. However the price for extreme accuracy can be expensive in CPU time. Alternatively, $F\left(n + \frac{1}{2}, \frac{1}{2}, n + 1 | p\right)$ can be evaluated using the Taylor expansion (34) which is faster and yet gives satisfactory results provided the plasma aspect ratio < 100. As a rule, we have found that the number of terms in the Taylor expansion must be typically $\sim 10/(1-p)$.

Note also that expressing the Green's function in hypergeometric function allows one to easily take the ballooning limit $n \to \infty$; the hypergeometric function then reduces to

$$F(n+\tfrac{1}{2},\tfrac{1}{2},n+1|p) \sim (1-p)^{-\frac{1}{2}}.$$

To compute $K = \partial_u G$, we make use of the following relations

$$\frac{\partial G}{\partial z} = \left(\frac{z'-z}{r'r}\right)(s^2-1)^{\frac{3}{2}}\frac{\partial G}{\partial s}, \tag{53}$$

$$\frac{\partial G}{\partial r} = -\frac{G}{2r} + \left(\frac{\lambda r'-r}{r'r}\right)(s^2-1)^{\frac{3}{2}}\frac{\partial G}{\partial s} \tag{54}$$

and

$$\frac{\partial G}{\partial s} = \frac{n+\frac{1}{2}}{(s^2-1)^{\frac{1}{2}}}\left[\frac{sG_n}{(s^2-1)^{\frac{1}{2}}} - G_{n+1}\right]. \tag{55}$$

6. Singularity as $\rho' \to \rho$

For $\boldsymbol{\rho}' \to \boldsymbol{\rho}$, we have $\lambda \to 1+$, $s \to \infty$ and

$$F\left(n+\tfrac{1}{2},\tfrac{1}{2},n+1|p\to 1-\right) \sim -\frac{\Gamma(n+1)}{\sqrt{\pi}\Gamma(n+\frac{1}{2})}\left[\log\frac{2}{s} + 2\gamma + \Psi(\tfrac{1}{2}) + \Psi(n+\tfrac{1}{2})\right. \tag{56}$$

$$\left. + \frac{n+\frac{1}{2}}{s}\log\frac{2}{s} + \mathcal{O}(1/s) + \mathcal{O}(\log s/s^2)\right] \tag{57}$$

where $\gamma = 0.577215665\cdots$ is Euler's constant and $\Psi(z) \equiv \Gamma'(z)/\Gamma(z)$. Hence,

$$G(\boldsymbol{\rho}', \boldsymbol{\rho}) \sim -\frac{1}{(r'r)^{\frac{1}{2}}}\log|\boldsymbol{\rho}'-\boldsymbol{\rho}| \sim -\frac{1}{\pi r'}\log|\theta'-\theta+2\pi k|; \quad k = \cdots,-1,0,1,\cdots \tag{58}$$

as $\boldsymbol{\rho}' \to \boldsymbol{\rho}$.

Although $\partial_z G$ and $\partial_r G$ have a $|\boldsymbol{\rho}'-\boldsymbol{\rho}|^{-1}$ singularity to leading order, this singularity cancels when combining Eqs. (53) and (54) to get $\partial_u G$. The first term on the right-hand side of (54) then yields

$$K(\theta',\theta) \sim -z_\theta\frac{G}{2r} \sim \frac{z_\theta}{2\pi r'^2}\log|\theta'-\theta+2\pi k|; \quad k = \cdots,-1,0,1,\cdots \tag{59}$$

as $\rho' \to \rho$.

The integrals in (50) and (51) must be evaluated carefully. We apply here the regularization prescription described by Chance [35], whereby the logarithmic terms $\log|\theta' - \theta|$, $\log|\theta' - \theta + 2\pi|$ and $\log|\theta' - \theta - 2\pi|$ are extracted from G and K and projected onto the e_i basis functions. The resulting integral is evaluated analytically; this is straightforward in the present case because the e_i's have finite support. The remaining (regularized) G and K are well behaved and their projection is determined using the two-point Gauss quadrature scheme within each (θ_i, θ_{i+1}) interval.

C. Matching across the resistive wall

We have up to now been only concerned with $\mathbf{B}$ on the vacuum side, with (48) providing a relation between the potential χ and its normal derivative at the contact of vacuum and wall. To obtain the boundary conditions for the plasma, we make use of

$$\begin{aligned} \mathbf{n}\cdot[[\mathbf{B}]] &= 0 \\ \mathbf{n}\times[[\mathbf{E}]] &= 0 \end{aligned} \tag{60}$$

where [[ ]] denotes the jump from the interior to exterior region. Furthermore we use $\nabla\times\nabla\times\mathbf{A} = \mathbf{J}$ within the wall and eliminate $\mathbf{J}$ in favour of the electric field $\mathbf{E} = -\partial_t\mathbf{A}$ by means of Ohm's law. The thin wall approximation allows us to neglect all surface derivatives with respect to the normal gradient ∂_n. We then get

$$[[\mathbf{B}_t]] = \frac{\tau_w}{a}\mathbf{E}\times\mathbf{n} \tag{61}$$

where $\mathbf{B}_t$ is the component of $\mathbf{B}$ tangent to the wall surface (i.e. $\mathbf{B} - \mathbf{n}\mathbf{n}\cdot\mathbf{B}$) and

$$\tau_w \equiv \delta\, a\, \sigma \tag{62}$$

denotes the characteristic wall time, δ being the wall thickness $\ll$ the minor radius a. Using the results of § IV B 1 and § IV B 2, the $\mathbf{B}$ field at the exterior is expressed as

$$\mathbf{B}_t^{ext} = \nabla_t\chi + k_a^{ext}\nabla\theta + k_b\nabla\phi + \frac{\partial\psi}{\partial u}\frac{\nabla\theta}{r} \tag{63}$$

whereas, at the interior contact surface, we have $\mathbf{B}_t = B_\theta^{int}\nabla\theta + B_\phi^{int}\nabla\phi$ which we assume to be given by the plasma equations. Here it is crucial to discriminate k_a just outside from its value just inside the wall:

$$[[k_a]] = \frac{\tau_w}{a}\frac{1}{2\pi}\oint \mathbf{E}_t\times\mathbf{n}\cdot dl \equiv \frac{\tau_w}{a}\langle \mathbf{E}_t\times\mathbf{n}\cdot\mathbf{x}_\theta\rangle \tag{64}$$

where Ohm's law has been used to determine the toroidal current flowing in the wall ($\mathbf{x}_\theta \equiv \partial_\theta\mathbf{x}$). This term can be moved to the right-hand side to yield

$$\mathbf{E}\times\mathbf{n}\cdot\mathbf{x}_\theta - \langle \mathbf{E}_t\times\mathbf{n}\cdot\mathbf{x}_\theta\rangle = \frac{a}{\tau_w}\left(\frac{\partial}{\partial\theta}V\,\rho_\theta\,\mathbf{B}\cdot\mathbf{n} + k_a^{int} + \frac{1}{r}\frac{\partial\psi}{\partial u} - B_\theta^{int}\right) \tag{65}$$

and

$$\mathbf{E}\times\mathbf{n}\cdot\mathbf{x}_\phi = \frac{a}{\tau_w}\left(\frac{\partial}{\partial\phi}V\,\rho_\theta\,\mathbf{B}\cdot\mathbf{n} + k_b - B_\phi^{int}\right) \tag{66}$$

after projecting onto $\mathbf{x}_\theta$ and $\mathbf{x}_\phi$, respectively. Equations (65) and (66) are the boundary conditions that the tangential electric field in the plasma is subjected to. The tangential and normal magnetic fields inside the plasma region should be considered as floating quantities, i.e. they automatically satisfy the proper boundary conditions through the electric field. All other quantities on the right-hand side are known from the interior: $k_{a,b}$ are given by (41), V by (49) and ψ by (28) - (31).

D. Implementation of the resistive wall boundary conditions into NIMROD

The present implementation of NIMROD includes the cold-plasma response only. In this limit, the equations condense into a generalized Faraday's law [36]

$$\Delta\mathbf{B} + \Delta t\nabla\times\,\mathsf{Z}\cdot\nabla\times\Delta\mathbf{B} = -\Delta t\nabla\times\mathbf{E}_{ex} \tag{67}$$

where $\mathbf{E}$ is explicit, i.e. it is computed at a previous time step. The second term in $\nabla\times\,\mathsf{Z}\cdot\nabla\times\Delta\mathbf{B}$ is the curl of the implicit part $\mathbf{E}_{im}$ of the electric field $\mathbf{E} = \mathbf{E}_{im} + \mathbf{E}_{ex}$, with the tensor Z playing the role of an impedance.

Updating $\mathbf{B} \rightarrow \mathbf{B}+\Delta\mathbf{B}$ requires the inversion of the $\mathbf{\Omega} = \mathsf{I} + \Delta t \nabla\times \mathsf{Z}\cdot\nabla\times \mathsf{I}$ operator. To do so

$$\left.\begin{aligned} \Delta\mathbf{B} &= \textstyle\sum_q \mathbf{B}_q \alpha_q(r,z,\phi) \\ -\nabla\times\mathbf{E}_{ex} &= \textstyle\sum_q \mathbf{R}_q \alpha_q(r,z,\phi) \end{aligned}\right\} \tag{68}$$

are expanded in finite elements in (r,z) and in Fourier modes along ϕ. Multiplying (67) by the basis function α_p and integrating over the plasma volume yields the set of matrix equations

$$\sum_q \left(\mathsf{M}_{pq} - \Delta t \mathsf{L}_{pq}\right)\cdot\mathbf{B}_q^* = \Delta t \sum_q \left(\mathsf{M}_{pq}\cdot\mathbf{R}_q - \mathsf{S}_{pq}\cdot\mathbf{B}_q\right) \tag{69}$$

where * denotes the new (implicit) value,

$$\mathsf{M}_{pq} = \int d\tau \alpha_p \alpha_q \tag{70}$$

is the "mass" matrix,

$$\mathsf{L}_{pq} = \int d\tau \nabla\alpha_p \times \mathsf{I} \cdot \mathsf{Z} \cdot \nabla\alpha_q \times \mathsf{I} \tag{71}$$

is the inductance matrix (so-called because it is related to the change in magnetic energy), and

$$\mathsf{S}_{pq} = \oint d\boldsymbol{\sigma} \times \alpha_p \, \mathsf{Z}\cdot\nabla\times\alpha_q\mathbf{B}_q \tag{72}$$

is the surface term arising from integrating by parts. Note that setting this term to zero is equivalent to having $\mathbf{E}\times\mathbf{n}$ zero at the boundary — these are the natural boundary conditions which the finite element method satisfies by default. All we have to do to generalize these boundary conditions in the presence of a resistive wall is to replace $\mathsf{Z}\cdot\nabla\times\alpha_q\mathbf{B}_q$ in (72) by (65) and (66). This can be done either implicitely or explicitely. Because the Green's function method couples all the nodes at the boundary through the (full) matrix V of (48), it is suggested that an explicit scheme whereby $\mathsf{Z}\cdot\nabla\times\alpha_q\mathbf{B}_q$ is replaced by the tangential field computed at the previous time step is desirable for numerical efficiency, and justified as long as the resitive wall time $\tau_w \gg \Delta t$ the time step.

E. Validation

A circular shaped plasma is considered with small radius a and major radius R. Using a coordinate transformation from (r, z) to (ρ, θ),

$$\left.\begin{aligned} r &= R(1 + \epsilon\rho\cos\theta) \\ z &= R\epsilon\rho\sin\theta \end{aligned}\right\}$$

the Laplacian operator in (40) takes the form

$$a^2\nabla^2\chi = \frac{1}{\rho}\frac{\partial}{\partial\rho}\rho\frac{\partial}{\partial\rho} + \frac{1}{\rho^2}\frac{\partial^2}{\partial\theta^2} - \epsilon^2 n^2 + \mathcal{O}(\epsilon).$$

As ϵ is varied, we have the toroidal mode number $n \propto \epsilon^{-1}$ to conserve the periodicity length along the toroidal angle. Thus, to leading order in ϵ, χ must satisfy a modified Bessel equation. Adopting a uniform χ on the surface of the wall we then have

$$V = -\frac{K_0(n\epsilon)}{n\epsilon K_1(n\epsilon)}$$

as an approximate solution as $\epsilon \to 0$.

In Fig. 18 ϵ has been varied from 0.5 to 0.001 and n from 1 to 20. We observe that the numerical solutions match precisely the asymptotic form in the large, and surprisingly, also in the small aspect ratio limit.

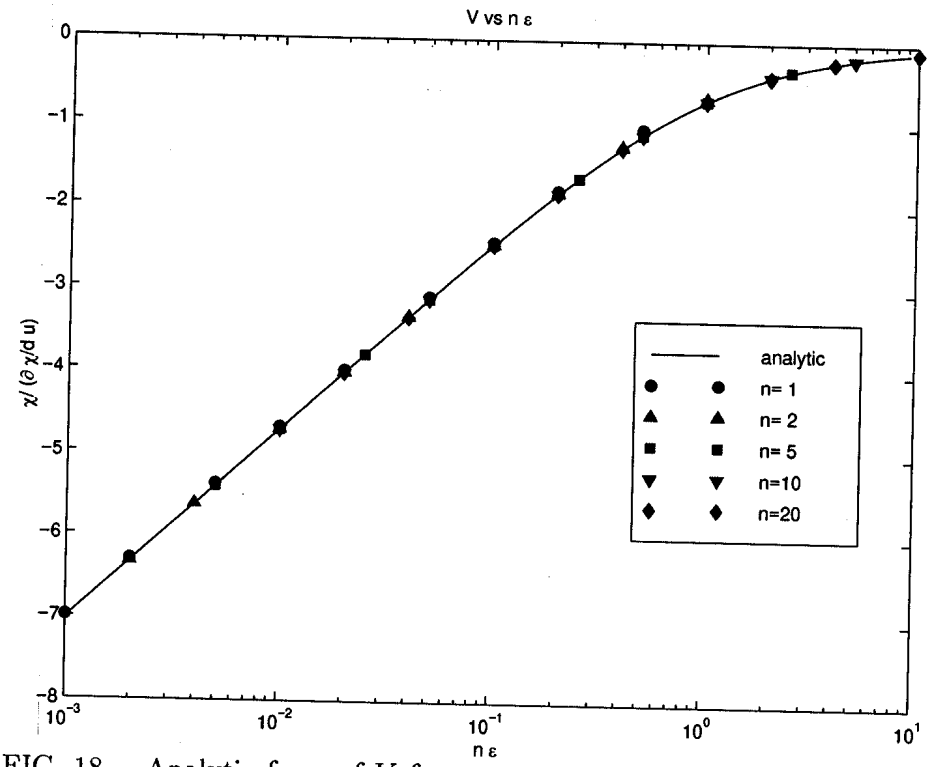

FIG. 18. Analytic form of V for $\chi = \text{const}$ over the surface and numerical results obtained using the WALL code with 128 nodes.

V. SUMMARY

In the first part of this report, it is shown that the tearing mode experiences a stabilizing mechanism during its growth, which is due to the flattening of the equilibrium profile and which is proportional to the island width w times $\log w$. This stabilization can produce a saturated island even when the matching index $\Delta' > 0$, which is often the case for the $m = 2, n = 1$ mode. It can also considerably reduces the saturation width of the $m = 3, n = 2$ mode, which tends to have a slightly negative Δ' and a strong bootstrap current drive. Because the flattening occurs on a length scale comparable to the island width, the resulting stabilization can be determined either as an outer region effect or within the inner layer equation. Both approaches give a similar dependence with a coefficient of proportionality of the order of two.

It appears from experimental evidences as well as from numerical simulations that the quasi-linear stabilization mechanism may turn out to be too weak to provide an acceptable saturation width for the 3/2, 2/1 and 4/3 modes in ITER. Thus we will have to rely on additional means to stabilize the mode, particularly at moderate to high β as pressure both increases the bootstrap current drive and Δ'. It is shown here that slight current profile modifications due to the application of a small localized current drive about a rational surface can make Δ' large and negative. Such a sensitivity can be explained by the fact that Δ' depends on the current density gradient near the singular (rational) surface rather than the current amplitude. Since the saturation width is approximately proportional to $(-\Delta')^{-1}$, the localized current drive stabilization can be very effective.

I have last May recently written a report "Stabilization of neoclassical tearing modes using a continuous localized current drive for ITER" on this subject, which contains additional results and which is available at `http://ppc41tc.iterus.org/~pletzea/reports.html`.

In the third part of this report I have developed a formalism for applying resistive wall boundary conditions to nonlinear restive codes such as NIMROD and MH3D. The approach is similar to the one used for linear codes; it is based on solving the plasma equation inside a

closed volume which is assumed to be toroidally symmetric. The plasma volume is bounded by a resistive wall, beyond which the magneto-static equations are solved using Green's functions. A new form of the Green's function based on the hypergeometric function has been found, which is numerically fast, accurate and also appropriate for taking the ballooning limit. A scalar potential representation is used for the magnetic field, both for axisymmetric and non-axisymmetric modes. In addition provision has been made to incorporate a driven response to toroidally symmetric external coils using a one-component potential vector field representation. It is proposed that the resistive wall boundary conditions be implemented as "natural" explicit boundary conditions into NIMROD, i.e. in the form of a surface term given by (72) with $Z \cdot \nabla \times \alpha_q \mathbf{B}_q$ replaced by the tangential electric field of Eqs. (65) and (66). The implementation into NIMROD remains to be done.

ACKNOWLEDGMENTS

This work was partly supported by the Swiss National Fund and Euratom.

I am particularly indebted to Rip Perkins for initiating the study of the effect of a continuous localized current drive on stability, to Marshall Rosenbluth for his contribution in obtaining (20) and to the NIMROD team for making their code available. Discussions with Dalton Schnack, Alfonso Tarditi and Carl Sovinec have been of great help in defining the best strategy to implement the resistive wall boundary conditions into NIMROD.

REFERENCES

[1] W. X. Qu and J. D. Callen, Report UWPR-85-5, University of Wisconsin (1985).

[2] R. Carrera, R. D. Hazeltine, and M. Kotschenreuther, Phys. Fluids **29**, 899 (1986).

[3] R. Fitzpatrick, Phys. Plasmas **2**, 825 (1995).

[4] H. R. Wilson, J. W. Connor, R. J. Hastie, and C. C. Hegna, Phys. Plasmas **3**, 248 (1996).

[5] R. J. L. Haye, private communication (1998).

[6] F. Porcelli, D. Boucher, and M. N. Rosenbluth, Plasma Phys. Contr. Fusion **38**, 2163 (1996).

[7] O. Sauter *et al.*, Phys. Plasmas **4**, 1654 (1996).

[8] A. Thyagaraja, Phys. Fluids **24**, 1716 (1981).

[9] R. B. White and D. A. Monticello, Phys. Fluids **20**, 800 (1977).

[10] F. Perkins, R. W. Harvey, M. Makowski, A. Pletzer and M. N. Rosenbluth, APS Poster (1997).

[11] C. C. Hegna and J. D. Callen, Phys. Plasmas **4**, 2940 (1997).

[12] H. Zohm, Phys. Plasmas **4**, 3433 (1997).

[13] J. Wesley *et al.*, in *Proceedings of the 16th IAEA Conference, Montreal* (1996).

[14] N. Pomphrey and W. Park, in *APS Denver* (1996).

[15] L. E. Zakharov, A. I. Smolyakov, and A. A. Subbotin, Sov. J. Plasma Phys. **16**, 451 (1991).

[16] W. A. Newcomb, Ann. Phys. **10**, 232 (1960).

[17] M. Bineau, Nucl. Fusion **2**, 130 (1962).

[18] R. L. Dewar and A. Pletzer, J. Plasma Phys. **43**, 291 (1990).

[19] Z. Chang *et al.*, Phys. Plasmas **5**, 450 (1998).

[20] P. H. Rutherford, Phys. Fluids **16**, 1903 (1973).

[21] M. Kotschenreuther, R. D. Hazeltine, and P. J. Morrison, Phys. Fluids **28**, 294 (1985).

[22] C. C. Hegna and J. D. Callen, Phys. Plasmas **1**, 3135 (1994).

[23] M. Zabiégo and X. Garbet, Phys. Plasmas **2**, 1236 (1995).

[24] Z. Chang *et al.*, Phys. Rev. Lett. **74**, 4663 (1995).

[25] A. Pletzer and R. L. Dewar, J. Plasmå Phys. **45**, 427 (1991).

[26] A. D. Miller and R. L. Dewar, J. Comput. Phys. **66**, 356 (1986).

[27] A. Pletzer, A. Bondeson, and R. L. Dewar, J. Comput. Phys. **115**, 530 (1994).

[28] A. H. Glasser, J. M. Greene, and J. L. Johnson, Phys. Fluids **18**, 875 (1975).

[29] A. Pletzer, in *Joint Varenna-Lausanne International Workshop held at Varenna*, edited by J. W. Connor, E. Sindoni, and J. Vaclavik (Editrice Compositori, Via Stalingrado 97/2 - 40128 Bologna, Italy, 1996).

[30] C. C. Hegna and J. D. Callen, Phys. Plasmas **1**, 2308 (1994).

[31] E. Westerhof, Nucl. Fusion **27**, 1929 (1987).

[32] R. Gruber *et al.*, Comput. Phys. Commun. **21**, 323 (1981).

[33] R. Lüst and E. Martensen, Z. Naturforsch. **15a**, 706 (1960).

[34] P. M. Morse and H. Feshbach, in *Methods of Theoretical Physics* (MacGraw-Hill, New York, 1953), p. 375.

[35] M. S. Chance, Phys. Plasmas **4**, 2161 (1997).

[36] D. D. Schnack and the NIMROD Team, Technical report, Science Applications International Corp., San Diego, CA 92121 (1998).